Aerospace Science and Technology 80 (2018) 520–540

Contents lists available at ScienceDirect

Aerospace Science and Technology

www.elsevier.com/locate/aescte

Verification and application of a mean flow perturbation method for jet noise

Swagata Bhaumik [a,*], Datta V. Gaitonde [b], S. Unnikrishnan [b], Aniruddha Sinha [c], Hao Shen [d]

[a] Department of Mechanical Engineering, Indian Institute of Technology Jammu, Jammu – 181221, India
[b] Department of Mechanical and Aerospace Engineering, The Ohio State University, Columbus, OH 43210, United States of America
[c] Department of Aerospace Engineering, Indian Institute of Technology Bombay, Mumbai – 400076, India
[d] Boeing Research and Technology, St. Louis, MO 63042, United States of America

ARTICLE INFO

Article history:
Received 28 July 2017
Received in revised form 11 March 2018
Accepted 26 June 2018
Available online 3 July 2018

Keywords:
Navier–Stokes equation
Stability analysis
Parabolized stability equation (PSE)
Linear stability theory (LST)
Global stability analysis
Large-eddy simulations

ABSTRACT

The stability properties of basic states are often elucidated by examining the evolution of small disturbances. Such studies have recently been successfully applied to mean turbulent states, obtained through averaging of experimental measurements or Large-Eddy Simulations (LES), for both wall-bounded as well as free shear flows. Typically, the equations are employed using the disturbance form of the equations. To circumvent the necessity to linearize the governing equations, an especially tedious task for viscous and turbulent closure terms, Touber and Sandham (2009) [21], proposed an approach that achieves the same purpose by solving the full Navier–Stokes (NS) equations, with a forcing term to maintain mean flow invariance. The method places no restrictions, such as slow streamwise variations, on the underlying basic state. The goals of the current work are to first verify this mean flow perturbation (NS-MFP) technique and then apply it to the problem of jet noise. For the first thrust, we show that when the basic state is appropriately constrained, the technique reverts to Linear, Parabolized and Global stability methods. The method is then verified by reproducing the growth of unstable modes in an inviscid Mach 6 entropy layer. The application to jet noise considers subsonic Mach 0.9 and perfectly expanded supersonic Mach 1.3 round jets. The results are compared with those from Parabolized Stability Equations (PSE) and LES solutions, respectively, considering monochromatic and multi-frequency perturbations. The NS-MFP method successfully reproduces key features of the modal response, including Strouhal number dependent directivity of noise radiation. Aspects related to the manner in which the mean basic state is obtained, whether from LES or Reynolds-averaged Navier–Stokes (RANS) equation are also explored. In particular, the sensitivity of the perturbation to whether the eddy viscosity is included or not, is examined in reference to maximum intensity of pressure fluctuation, directivity of noise radiation and the rate of fall-off of the spectra at higher Strouhal numbers. The results indicate that a closer match on the noise-radiation characteristics is obtained when effects of eddy-viscosity on the disturbances are neglected.

1. Introduction

The growth and propagation of perturbations in a flow can provide key insights into its behavior. Steady flow-fields are typically considered for this purpose. A comprehensive review of various methods employed to analyze the stability of laminar flow-fields may be found in Ref. [1]. One of the simpler approaches obtains the eigen-solution of linear stability theory (LST) equations, which assumes that the flow (basic state) does not vary in the streamwise direction. A more sophisticated method is that based on the Parabolized Stability Equations (PSE) [2,3], which allows for inhomogeneous conditions, and has been used to explore linear [4] and non-linear [5] disturbance growth mechanisms in free and wall-bounded shear flows. PSE essentially tracks the evolution of downstream propagating perturbation modes, but is limited to slow streamwise variation of the basic state. There is also the consideration of "remaining ellipticity" [6,7], which can influence the accuracy of the results. Though classical PSE has been developed for 2D flows [4], it has also been applied to 3D axisymmetric flows [8,9], shear-layers with spanwise periodicity [10] and the mean turbulent subsonic jet issuing from serrated (chevroned) nozzles [11]. Global Stability Theory (GST) [1,12,13] lifts constraints of the re-

---

[*] Corresponding author.
E-mail address: swagatameister@gmail.com (S. Bhaumik).

https://doi.org/10.1016/j.ast.2018.06.027

quirement of slow streamwise variation in PSE, but is significantly more expensive for full 3D flow problems.

As a compromise, an extension of PSE called PSE-3D has been developed as a branch of global stability analysis which addresses some of the limitations of classic PSE without resorting to full Tri-Global stability analysis for quasi-3D flows [14,15]. For such problems, while a Bi-Global stability analysis is performed at the inlet of the domain to determine the eigenfunctions and its growth-rates, its subsequent streamwise evolution is computed by PSE, requiring that the flow should be slowly varying along that direction [14,15]. Some shortcomings of PSE have been overcome in the recently proposed one-way approximation of hyperbolic equations in Towne and Colonius [16], where the upstream propagating modes are systematically removed from the equations.

Although inviscid or viscous stability theories have been developed for laminar steady basic states, recent applications to mean (time-invariant) turbulent flow have yielded considerable insight into the dynamics. In nominally 2-D turbulent shock-wave boundary layer interactions (SBLI), such as those arising from impinging shocks or compression corners, these fields display a dominant low-frequency component at scales far separated from those associated with turbulent fluctuations. Numerous mechanisms have been proposed to explain this phenomenon, including larger-scale events in the incoming flow [17], Kelvin–Helmholtz based oscillation of the separated shear layer [18] and amplification of incoming signals by the separation bubble [19,20]. The method under consideration in this work, the Navier–Stokes based Mean Flow Perturbation method (NS-MFP), was introduced by Touber and Sandham [21] to reproduce the key elements of the low frequency unsteadiness by perturbing the mean flow from a Large-Eddy Simulation (LES).

The use of a mean flow to generate insight into the unsteady turbulent dynamics has also seen significant success in key aspects of jet noise predictions. The relevant theory that broadly connects sound generation processes to the stability of the flow is mature. For example, in a review article, Tam [22] notes that 'large-scale turbulent fluctuations of a statistically stationary flow can be mathematically represented by a linear superposition of its normal modes' and that these structures contribute significantly to the noise field. Other efforts building on this construct may be found in stochastic instability wave models of Refs. [23–25].

Noise prediction models based on instability mechanisms of turbulent mean flows have been advanced recently in several efforts. For example, Refs. [26,27] show that the evolution of lower frequency components follows from the linear instability of the mean flow, as obtained through PSE. The mean of the turbulent jet for PSE, is either obtained from PIV measurements [26] or from validated LES computations [8]. In Ref. [8], it is shown that peak aft direction noise for a supersonic Mach 1.5 jet filtered by Proper Orthogonal Decomposition (POD) techniques can be satisfactorily predicted by a combination of PSE modes combined with a near-to-far field transformation. However, there are limitations of linearized instability analysis of the mean turbulent flow-field to predict noise radiation characteristics. For example, Ref. [28] notes that low-frequency perturbations generated due to nonlinear interactions of spatially unstable modes are more effective in noise-radiation at shallow polar angles when compared to the instability wave at the same frequency.

In the present work, we focus on first verifying the approach of Touber and Sandham [21] and subsequently adapting it to the analysis of jets. Typical techniques to explore perturbation propagation solve the disturbance form of the governing equations *i.e.,* where the basic state, assumed to satisfy the Navier–Stokes equations, forms the coefficients of the disturbance equation. Focusing on those in use for computational aeroacoustics, these include the generalized acoustic analogy (GAA) [29], linearized Euler equation (LEE) [30], compact disturbance equation (CDE) [31] and zero-averaged source term (ZAST) in nonlinear residual (disturbance) equation [32]. In the generalized acoustic analogy (GAA) [29] and linearized Euler equations (LEE) [30] linearization is performed about the statistically stationary mean-flow, while requiring that these also satisfy inhomogeneous NSE. However, in the nonlinear disturbance equations (NLDE) [33], compact disturbance equation (CDE) [31] and zero-averaged source term (ZAST) [32] approaches, the nonlinear disturbance equations are retained.

The NS-MFP approach does not solve the disturbance equations: rather, the Navier–Stokes equations are solved with a forcing term to maintain the invariance of the basic state (Section 2), and operations are performed on the total variable instead of the disturbance. An advantage of this approach is that the complexity of treating the viscous and turbulent closure terms, which are often neglected in approaches that solve the disturbance equations, is circumvented. Furthermore, since the full Navier–Stokes operator is considered, no constraints are placed on streamwise variation rates such as those enforced on PSE, thus facilitating application even to flows with shocks. Because it can be implemented in existing NS codes in a straightforward manner, it is also relatively easy to extend to three-dimensions [34]. The method thus has the potential to treat relatively complex flows for which acceptable computed mean solutions are available. Such solutions could be obtained for example from experimentally anchored Reynolds Averaged Navier Stokes (RANS) equations such as those of Ref. [35] for 3-D SBLI using tailored turbulence models. NS-MFP thus provides the opportunity to analyze unsteady aspects of 3-D flows without expensive direct numerical simulations (DNS) or LES or difficult-to-obtain 3-D volumetric measured data. Moreover, unlike LST, PSE or GST, NS-MFP method does not neglect the nonlinear interaction among various perturbation modes, which under certain circumstances can also provide valuable insight into the flow physics [28].

The key step in NS-MFP is to pre-compute the change in the solution vector when the NS operator is applied to the basic state. A disturbance is then introduced and marched in time together with the basic state with the same NS operator. After each step however, the pre-computed difference in the basic state is subtracted (this step may be viewed as a forcing term) to ensure that it does not vary with time, leaving only the changes associated with the disturbance. Since the NS-MFP approach poses an initial-boundary value problem for the disturbance evolution, it is relatively efficient (Section 3 contains comments on the computational cost) compared to methods that seek the eigenmodes. However, a heuristic approach using different perturbations is necessary to derive a comprehensive assessment of disturbance growth.

Although the method has been successfully applied to SBLI, it has not been systematically verified by comparison to classical solutions. We perform such an analysis in two different ways as a first step of our work. First, we show theoretically that under appropriate conditions, NS-MFP reverts to LST, PSE and GST (Section 3). The results are confirmed by demonstrating that NS-MFP reproduces LST results for a Mach 6 entropy layer (Section 4). We then apply the method to turbulent jet flow, with the goal of reproducing principal aspects of jet noise. Although the ultimate goal is to apply the technique to jets with shock waves, for the present work, we limit the scope to ideally expanded conditions. For generality, we consider a subsonic (Mach 0.9) and a supersonic (Mach 1.3) condition. For the former, we examine the conditions under which NS-MFP recovers the PSE solution, with both methods using a time-averaged LES solution as the basic state. For the Mach 1.3 case, we consider NS-MFP when the base-flow is obtained from both LES and RANS and use well-validated LES as the truth model. We use this case to also address a key point of interest on the effect of eddy viscosity on disturbance evolution.

2. The Navier–Stokes-based mean flow perturbation method

A brief description of the method to predict disturbance evolution in a steady basic state is first provided. Let Q be the vector composed of the basic state, Q_b, and added perturbations Q', *i.e.*, $Q = Q_b + Q'$. The temporal evolution of Q is obtained by solving the full non-linear Navier–Stokes equation as

$$\frac{\partial Q}{\partial t} = L(Q) \tag{1}$$

where, L includes all spatial derivatives (advection and diffusion terms). If the base-flow Q_b is used as the initial condition to the Navier–Stokes solver (without imposing any perturbations) then:

$$\frac{\partial Q_b}{\partial t} = L(Q_b) \tag{2}$$

Q_b may not itself satisfy the NS equations, $\frac{\partial Q_b}{\partial t} \neq 0$, as for example, when obtained through time-averaging an LES or measurement data. The evolution equation for the imposed disturbance Q' is obtained by subtracting Eq. (2) from Eq. (1):

$$\frac{\partial Q'}{\partial t} = L(Q) - L(Q_b) \tag{3}$$

Thus $L(Q_b)$ acts as a forcing term in the governing evolution equation of Q'. Although we restrict our attention to linear situations, nonlinear interactions of disturbances are not explicitly neglected in Eq. (3). Note that disturbance equations directly solve Eqn. (3) by establishing the proper expressions for the left side of the equations (Q' is advanced directly), while the NS-MFP method achieves the same objective by evaluating the right hand side using the total variable Q.

$\Delta Q_b = Q^1 - Q^0$ is the change in the base-flow Q_b after it has been advanced by a single step (without any imposed disturbance): this quantity is precomputed and stored. For all subsequent time steps, it is then employed as a forcing term to ensure that Q_b does not change. ΔQ_b is zero if a laminar basic state is considered, as is a RANS-derived basic state if the effects of the eddy viscosity on the evolution of the disturbance are included (see Section 5.3 for a discussion of this aspect). However, $\Delta Q_b \neq 0$ when the basic state is a time-averaged LES or is obtained from PIV. Without the forcing term, this basic state exhibits a *drift*, which alters the characteristics of disturbance evolution. The NS-MFP technique thus facilitates the use of the total variable to obtain the evolution of disturbances, even if the basic state does not satisfy the Navier–Stokes equations.

Although the need for a forcing term is a drawback relative to solving the disturbance equations, there are several advantages to this approach. Since the operator L in Eqs. (1) through (3) considers all pertinent terms, including viscous fluxes as well as any turbulence closures, their effects are included in the evolution of the disturbance without the need to explicitly derive and implement these terms. The benefit is particularly important for turbulent closures, whose linearization can be tedious and model dependent (see e.g., Ref. [36], which performs these operations for a specific model) or unknown, as in the case of implicit LES approaches as employed in Ref. [37]. Furthermore, ΔQ_b, and indeed the evolution of Eq. (2), is independent of the method employed for the LES or RANS from which the mean basic state is derived. This permits the scheme for the NS-MFP to be different from that used in LES/RANS and facilitates the use of highly accurate schemes that can correctly track small imposed perturbations even through shock waves.

The Navier–Stokes equations are solved in non-dimensional form on a curvilinear (ξ, η, ζ)-coordinate system:

$$\frac{\partial}{\partial \tau}\left(\frac{Q}{J}\right) = \left[-\left(\frac{\partial F_i}{\partial \xi} + \frac{\partial G_i}{\partial \eta} + \frac{\partial H_i}{\partial \zeta}\right) + \frac{1}{Re}\left(\frac{\partial F_v}{\partial \xi} + \frac{\partial G_v}{\partial \eta} + \frac{\partial H_v}{\partial \zeta}\right)\right] \tag{4}$$

where, $Q = [\rho, \rho u, \rho v, \rho w, \rho E]^T$ denotes the solution vector, defined in terms of the fluid density ρ, Cartesian velocity components (u, v, w) and total specific internal energy $E = T/(\gamma - 1)M^2 + (u^2 + v^2 + w^2)/2$. Here, M is the Mach number of the flow, γ is the ratio of the specific heats and T is the fluid temperature. Additionally, we have used the ideal gas law to connect fluid-pressure p to ρ and T as $p = \rho T/\gamma M^2$. Sutherland's law is used to express fluid viscosity μ as a function of temperature T.

In Eq. (4), $J = \partial(\xi, \eta, \zeta, \tau)/\partial(x, y, z, t)$ denotes the Jacobian of the transformation from Cartesian (x, y, z) to curvilinear (ξ, η, ζ)-coordinate system. The inviscid and viscous fluxes in (ξ, η, ζ)-directions are represented in Eq. (4) by (F_i, G_i, H_i) and (F_v, G_v, H_v), respectively. The expression for the inviscid flux F_i is given as

$$F_i = \begin{bmatrix} \rho U \\ \rho u U + \widehat{\xi}_x p \\ \rho v U + \widehat{\xi}_y p \\ \rho w U + \widehat{\xi}_z p \\ (\rho E + p)U - \widehat{\xi}_t p \end{bmatrix} \tag{5}$$

where $U = (\widehat{\xi}_t + \widehat{\xi}_x u + \widehat{\xi}_y v + \widehat{\xi}_z w)$, $\widehat{\xi}_x = J^{-1}\partial\xi/\partial x$, $\widehat{\xi}_y = J^{-1}\partial\xi/\partial y$ and $\widehat{\xi}_z = J^{-1}\partial\xi/\partial z$. The viscous flux F_v is given as

$$F_v = \begin{bmatrix} 0 \\ \widehat{\xi}_{x_i}\tau_{i1} \\ \widehat{\xi}_{x_i}\tau_{i2} \\ \widehat{\xi}_{x_i}\tau_{i3} \\ \widehat{\xi}_{x_i}(u_j\tau_{ij} + \frac{1}{(\gamma-1)M^2}\frac{1}{Pr}q_i \end{bmatrix} \tag{6}$$

where the Einstein summation convention is used and Pr denotes the Prandtl number of the fluid. The stress tensor τ_{ij} and heat flux q_i appearing in Eq. (6) are given as

$$\tau_{ij} = \mu\left(\frac{\partial \xi_k}{\partial x_j}\frac{\partial u_i}{\partial \xi_k} + \frac{\partial \xi_k}{\partial x_i}\frac{\partial u_j}{\partial \xi_k} - \frac{2}{3}\delta_{ij}\frac{\partial \xi_l}{\partial x_k}\frac{\partial u_k}{\partial \xi_l}\right) \tag{7}$$

$$q_i = \kappa \frac{\partial \xi_j}{\partial x_i}\frac{\partial T}{\partial \xi_j} \tag{8}$$

Similar expressions for G_i, H_i, G_v and H_v can be obtained by replacing ξ by η and ζ in Eqs. (5) and (6), respectively.

Since NS-MFP maintains the basic state, no boundary conditions are applied when computing ΔQ_b. At subsequent steps, the disturbance is introduced on one of the boundaries, and conditions on the remaining boundaries are only applied to disturbance quantities. The disturbances introduced are different for the entropy layer and jet cases and are discussed in the context of each problem below. The computational cost of each step in the procedure is essentially the same as for an iteration in the underlying Navier–Stokes operator and is discussed below.

3. Properties of NS-MFP

To gain insight into the approach, we first investigate the manner in which the NS-MFP approach relaxes to other well-known stability methods. Although details are deferred to the Appendix, it is instructive to explicitly show the connection between the basic state and perturbed quantities. In NS-MFP, the time-updated perturbations are obtained as the difference between the changes in the base-flow Q_b and the total flow $Q = Q_b + Q'$ when both are subjected to the Navier–Stokes operator (4) as explained in Sec. 2. Effectively, the equations governing Q', obtained from Eq. (4), are the linearized Navier–Stokes equations, except that the solution procedure uses Q in appropriate fashion (see discussions in Sec. 2):

$$\frac{\partial}{\partial \tau}\left(\frac{Q'}{J}\right) = \left[-\left(\frac{\partial F_i'}{\partial \xi} + \frac{\partial G_i'}{\partial \eta} + \frac{\partial H_i'}{\partial \zeta}\right) + \frac{1}{Re}\left(\frac{\partial F_v'}{\partial \xi} + \frac{\partial G_v'}{\partial \eta} + \frac{\partial H_v'}{\partial \zeta}\right)\right] \tag{9}$$

The expression for perturbation inviscid flux $F_i' = F_i - F_{i_b}$ can be given as

$$F_i' = \begin{bmatrix} \rho_b U' + \rho' U_b + \rho' U' \\ \rho_b u_b U' + \rho_b u' U_b + \rho' u_b U_b + \rho_b u' U' + \rho' u_b U_b + \rho_b u_b U' + \rho' u' U' + \widehat{\xi}_x p' \\ \rho_b v_b U' + \rho_b v' U_b + \rho' v_b U_b + \rho_b v' U' + \rho' v_b U_b + \rho_b v_b U' + \rho' v' U' + \widehat{\xi}_y p' \\ \rho_b w_b U' + \rho_b w' U_b + \rho' w_b U_b + \rho_b w' U' + \rho' w_b U_b + \rho_b w_b U' + \rho' w' U' + \widehat{\xi}_z p' \\ (\rho_b E_b + p_b) U' + (\rho' E_b + \rho_b E' + \rho' E' + p') U_b + (\rho' E_b + \rho_b E' + \rho' E' + p') U' - \widehat{\xi}_t p' \end{bmatrix} \tag{10}$$

where $U' = (\widehat{\xi}_x u' + \widehat{\xi}_y v' + \widehat{\xi}_z w')$, $\widehat{\xi}_x = J^{-1}\partial\xi/\partial x$, $\widehat{\xi}_y = J^{-1}\partial\xi/\partial y$, $\widehat{\xi}_z = J^{-1}\partial\xi/\partial z$ and

$$E' = T'/(\gamma - 1)M^2 + (u'u_b + v'v_b + w'w_b) + ({u'}^2 + {v'}^2 + {w'}^2)/2$$

The perturbation viscous flux $F_v' = F_v - F_{v_b}$ is given as

$$F_v' = \begin{bmatrix} 0 \\ \widehat{\xi}_{x_i} \tau_{i1}' \\ \widehat{\xi}_{x_i} \tau_{i2}' \\ \widehat{\xi}_{x_i} \tau_{i3}' \\ \widehat{\xi}_{x_i} (u_j' \tau_{ij_b} + u_{j_b} \tau_{ij}' + u_j' \tau_{ij}' + \frac{1}{(\gamma-1)M^2} \frac{1}{Pr} q_i') \end{bmatrix} \tag{11}$$

The perturbation stress tensor τ_{ij}' and heat flux q_i' appearing in Eq. (11) are:

$$\tau_{ij}' = \mu_b s_{ij}' + \mu' s_{ij_b} + \mu' s_{ij}' \tag{12}$$

$$q_i = \kappa_b \frac{\partial \xi_j}{\partial x_i}\frac{\partial T'}{\partial \xi_j} + \kappa' \frac{\partial \xi_j}{\partial x_i}\frac{\partial T_b}{\partial \xi_j} + \kappa' \frac{\partial \xi_j}{\partial x_i}\frac{\partial T'}{\partial \xi_j} \tag{13}$$

where s_{ij}' and s_{ij_b} denote perturbation and mean strain-rates, respectively:

$$s_{ij}' = \left[\left(\frac{\partial \xi_k}{\partial x_j}\frac{\partial u_i'}{\partial \xi_k} + \frac{\partial \xi_k}{\partial x_i}\frac{\partial u_j'}{\partial \xi_k} - \frac{2}{3}\delta_{ij}\frac{\partial \xi_l}{\partial x_k}\frac{\partial u_k'}{\partial \xi_l}\right)\right] \tag{14}$$

$$s_{ij_b} = \left[\left(\frac{\partial \xi_k}{\partial x_j}\frac{\partial u_{i_b}}{\partial \xi_k} + \frac{\partial \xi_k}{\partial x_i}\frac{\partial u_{j_b}}{\partial \xi_k} - \frac{2}{3}\delta_{ij}\frac{\partial \xi_l}{\partial x_k}\frac{\partial u_{k_b}}{\partial \xi_l}\right)\right] \tag{15}$$

Expressions for G_i', H_i', G_v' and H_v' can be defined by replacing ξ in Eqs. (10) and (11) by η and ζ, respectively.

The evolution of the disturbance is affected by both linear as well as non-linear terms *i.e.*, products of perturbation quantities. Thus, the forcing term associated with $L(Q_b)$, is generated by the NS operator, whereas when the disturbance equation is solved as for example in the NLDE approach, constancy of the basic state is assured simply by maintaining the coefficients (which are based on the basic state) constant. If the disturbances grow to non-linear levels, then the possibility must be considered that such growth could be the effect of a changing mean state (due to wave-induced stresses caused by non-zero mean of the disturbances [32]) combined with a linear disturbance growth subjected to the altered mean flow (secondary instability). Suponitsky et al. [28] discuss some considerations in this regard in the context of noise radiated by subsonic jets.

If it is assumed that the perturbation quantities in Eq. (9) are much smaller than corresponding variables in the base-flow, then the nonlinear disturbance terms in Eq. (9) can be neglected. The resulting linearized Navier–Stokes equation in terms of primitive variables in the physical (x, y, z)-coordinate system can be written symbolically as,

$$\begin{aligned} \frac{\partial W'}{\partial t} &= A_{11b}\frac{\partial W'}{\partial x} + A_{12b}\frac{\partial W'}{\partial y} + A_{13b}\frac{\partial W'}{\partial z} \\ &\quad + W'\left(\frac{\partial B_{11b}}{\partial x} + \frac{\partial B_{12b}}{\partial y} + \frac{\partial B_{13b}}{\partial z}\right) + C_{11b}\frac{\partial^2 W'}{\partial x^2} \\ &\quad + C_{12b}\frac{\partial^2 W'}{\partial y^2} + C_{13b}\frac{\partial^2 W'}{\partial z^2} + C_{14b}\frac{\partial^2 W'}{\partial x \partial y} \\ &\quad + C_{15b}\frac{\partial^2 W'}{\partial x \partial z} + C_{16b}\frac{\partial^2 W'}{\partial y \partial z} \end{aligned} \tag{16}$$

where, $W_b = [\rho_b, u_b, v_b, w_b, T_b]^T$ and $W' = [\rho', u', v', w', T']^T$ denote base-flow and disturbance quantities in primitive variables, respectively. In Eq. (16), the matrices $A_{..b}$, $B_{..b}$ and $C_{..b}$ are all functions of the base-flow variable W_b and its spatial derivatives.

The above elaboration of the NS-MFP method facilitates examination of its properties under different conditions which form the basis of traditional stability approaches. By enforcing various conditions on the basic state, it can be shown that the NS-MFP recovers these classical techniques. Details of the manner in which the method recovers local linear stability [38–40], parabolized stability equations [3,4] and the global stability approach [1,41] are provided in Appendix A.

The solution of Eq. (3) requires spatial and temporal discretization in a manner similar to those employed for the underlying LES, DNS or RANS. Therefore, the computational cost *per iteration* of NS-MFP is similar to those methods. Several considerations reduce the total requirement substantially however. First, the time to propagate the disturbance through the domain and acquire statistical data is much smaller than that required to obtain a statistically stationary turbulent state for the LES. Second, simplifications associated with 2-D or axisymmetry can often be leveraged if the disturbances are also of lower dimension. Finally, the scales in mean flow are much larger than those of the underlying turbulence. A coarser mesh than employed for the original flow, with suitable interpolation, may also then be appropriate. NS-MFP is thus much cheaper than LES or GST, for which estimates are provided in [1] but more expensive than PSE.

4. Disturbance growth in an entropy layer

We verify the approach and its implementation by considering the inviscid instability of the entropy layer evolving over a flat plate with a blunt nose (Fig. 1(a)). The region of interest L is $1 < \frac{L}{r} < Re_r$ where $Re_r = \rho_\infty U_\infty r/\mu_\infty$ is the Reynolds number based on the leading edge radius, r and ρ_∞, U_∞ and μ_∞ denote free-stream values of fluid density, velocity and viscosity, respectively. The inviscid instability is associated with the generalized inflection point, which is a sufficient condition to support unstable perturbations [42].

Analytical expressions for the leading order terms of the base-flow profiles of velocity and temperature (nondimensionalized by respective free-stream values) are [42–44]:

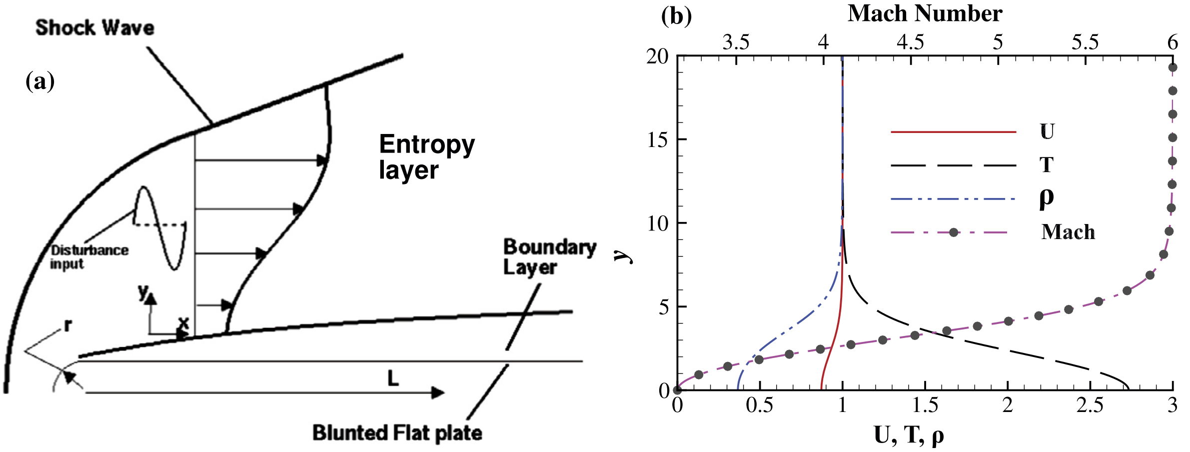

Fig. 1. (a) Schematic of blunted plate configuration and domain of interest. (b) Base-flow profiles of U velocity, density ρ, temperature T and Mach number plotted as functions of y-coordinate.

$$T(y) = \left[1 - \frac{2(M_\infty^2 - 1)^2}{M_\infty^2(\gamma+1)(M_\infty^2 - 1 + \psi^2)}\right] \times \left[1 + \frac{2\gamma(M_\infty^2 - 1)^2}{(\gamma+1)(M_\infty^2 - 1 + M_\infty^2\psi^2)}\right]^{1/\gamma} \tag{17}$$

$$U(y) = \left[1 - \frac{2(T-1)}{(\gamma-1)M_\infty^2}\right]^{1/2} \tag{18}$$

$$y = \int_0^\psi \frac{T}{U}\, d\psi \tag{19}$$

where M_∞ is the free-stream Mach number and $\gamma = 1.4$ for air. In Eqs. (17) and (18), the independent variable ψ is defined from Eq. (19). Equations (17) and (18) suggest that to leading order, temperature and velocity profiles are independent of the streamwise coordinate x. The streamwise variation of the base-flow variables only enter through the higher order terms which are neglected here. The pressure is assumed to be uniform inside the entropy layer and therefore, nondimensional density $\rho(y)$ and temperature $T(y)$ satisfy the ideal gas equation, $\rho(y)T(y) = 1$. The wall-normal velocity component V does not contribute any term to the leading order of the asymptotic expansion of the entropy layer profiles [43,44] and is therefore assumed to be zero. The profiles of the basic state mean velocity U, density ρ, temperature T and Mach number M for free-stream Mach number $M_\infty = 6$ are shown in Fig. 1(b).

Since the base-flow profiles are functions of the wall-normal coordinate y only, with $V(y) = 0$, the parallel flow approximation holds (where the streamwise variation of the base-flow quantities are neglected). Furthermore, since the current emphasis is on the investigation of the characteristics of 2-D disturbances, the transverse velocity component W is also assumed to be zero. The entropy layer velocity profile shown in Fig. 1(b) contains a generalized inflection point at $y = 2.775$ where $\partial[(\partial U/\partial y)/T]/\partial y = 0$. Normal mode analysis of perturbations yields system of ODEs for the eigen-solution of the perturbation evolution as [42]:

$$\frac{d\phi_0}{dy} - \frac{dU}{dy}\frac{\phi_0}{(U-c)} + i\alpha\frac{(U-c)}{\gamma}\left[1 - \frac{T}{M_\infty^2(U-c)^2}\right]\pi_0 = 0 \tag{20}$$

$$\frac{d\pi_0}{dy} + i\gamma M_\infty^2\,\alpha\,\frac{(U-c)}{T}\phi_0 = 0 \tag{21}$$

Table 1
Disturbance properties for indicated frequencies of excitation tabulated which are obtained from the linear inviscid instability analysis of the entropy layer. Here, c_r and c_i are the real and imaginary part of the complex phase speed $c = \omega/\alpha$.

ω	α_r	α_i	c_r	c_i	y_{cr}
0.0315	0.03476	-0.7745×10^{-3}	0.9057	0.2018×10^{-1}	1.754
0.145	0.1555	-0.2298×10^{-2}	0.9324	0.1378×10^{-1}	2.51
0.25	0.2659	-0.1152×10^{-2}	0.9402	0.4074×10^{-2}	2.73

where α and ω are complex wavenumber and circular frequency, respectively, while $c = \omega/\alpha$. The real part of c denotes the phase speed of the disturbances. The eigenfunctions ϕ_0 and π_0, representing v' and p', respectively, also satisfy the homogeneous boundary conditions:

$$(\phi_0, \pi_0) \longrightarrow 0, \quad \text{as} \quad y \longrightarrow \infty \quad \text{and} \quad \phi_0 = 0, \quad \text{at} \quad y = 0 \tag{22}$$

u', T' and ρ' can then be evaluated from the linearized inviscid u-momentum, energy and continuity equations, respectively. For excitation with real frequencies (*i.e.*, when ω is real), the spatial growth of the disturbance can be represented as $exp(-\alpha_i x)$ at wavelength $2\pi/\alpha_r$.

Although numerous simulations were performed, we distill the results by considering three distinct frequencies $\omega = 0.0315$, 0.145 and 0.25. The corresponding eigensystem for each was obtained by solving the eigenvalue problem, Eqs. (20)–(22) using the 4th-order Runge–Kutta integration scheme. The key properties of these disturbances are listed in Table 1 where, α_r is the disturbance wavenumber, α_i is the spatial amplification rate of the disturbances, (c_r, c_i) are the real and imaginary parts of the complex phase speed $c = (\omega/\alpha)$ and y_{cr} is the location of the critical layer, *i.e.*, where $(U - c_r) = 0$. The frequency $\omega = 0.145$ displays the maximum rate of amplification [42] in the range of unstable frequencies, whereas $\omega = 0.0315$ and 0.25 are located very close to the lower and upper bound of the unstable frequency range, consistent with the results of Ref. [42]. Fig. 2 shows the eigen-solution properties for $\omega = 0.145$. The real and imaginary parts of the temperature eigenfunction display rapid variation in the neighborhood of the critical layer y_{cr}. Other two non-optimal frequency cases considered here, *i.e.*, $\omega = 0.25$ and 0.0315, also show similar profile of eigenfunction and therefore are not shown here. For verification of MFP, the disturbances are introduced at the upstream boundary (see below) and the computed growth rate is compared with the theoretical value.

The computational domain is shown in Fig. 3. The basic state is constructed on this rectangular domain of streamwise length 400 units corresponding to approximately 9.87 wavelengths of the $\omega = 0.145$ case. The height of the domain is 20 units. 400 and 800 uniformly spaced mesh points are respectively employed in ξ-

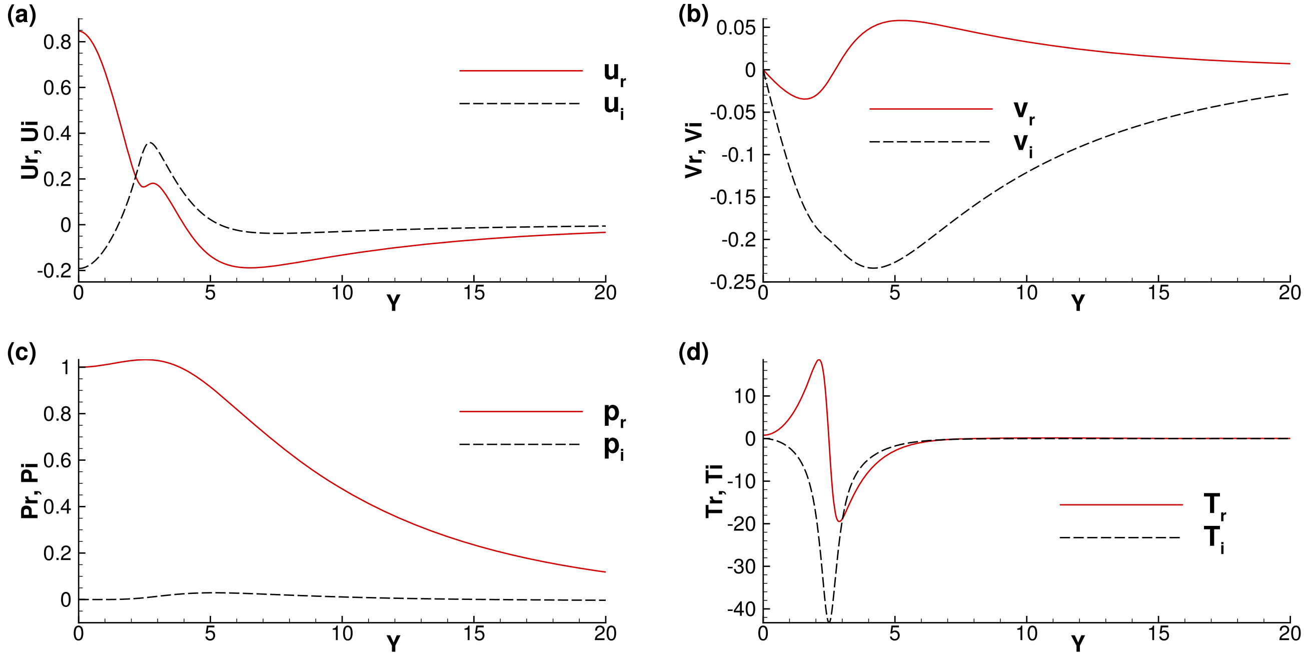

Fig. 2. Real and imaginary part of the disturbance u, v, p and T are shown for $\omega = 0.145$ in frames (a–d), respectively. These eigen-solutions are obtained by solving the inviscid instability equation given by Eqs. (20) and (21).

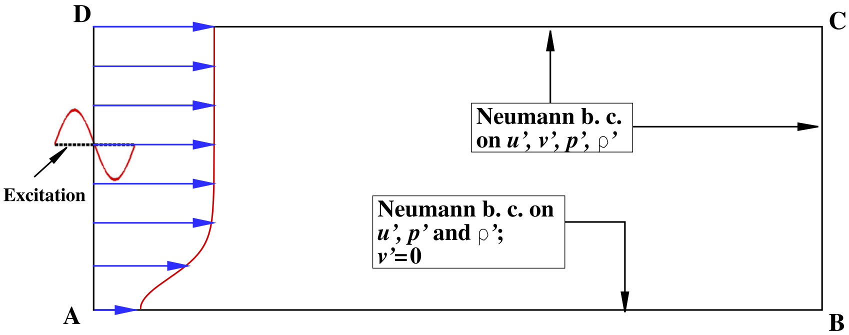

Fig. 3. Schematic diagram of the computational domain along with applied boundary conditions for NS-MFP.

and η-directions. Since the problem is inviscid and no discontinuities exist in the flow, the Euler subset of the NS-MFP equations is solved with the sixth-order compact-difference scheme of Ref. [45]. The derivatives of the inviscid fluxes are obtained by first forming the fluxes at the nodes and subsequently differentiating each component. A trace amount of fourth-order dissipation is added to systematically remove the spurious numerical disturbances in the solution. Time-integration of the solution is performed by the low-storage form of the fourth-order classical Runge–Kutta method [46]. A non-dimensional time-step of $\Delta t = 10^{-2}$ is used for the computations.

The disturbance is imposed at the inflow of the computational domain (segment AD of Fig. 3) by specifying the eigen-solution (obtained by solving Eqs. (20)–(22)) for the specified excitation frequency case:

$$\varphi'(0, y, t) = A \times \mathbb{R}\left(\varphi_0(y)\, e^{i\omega t}\right) \tag{23}$$

where $\mathbb{R}(\cdot)$ denotes the real part of the complex quantity $(\cdot)$ while φ' and φ_0 represent any of the quantities from u', v', p' and ρ' and the corresponding eigen-solution, respectively. The variable A in Eq. (23) denotes the amplitude of the imposed perturbation. At the outflow and the upper boundaries of the computational domain (segments BC and CD of Fig. 3) Neumann conditions are applied on disturbance quantities (u', v', p' and ρ') as

$$\frac{\partial q'}{\partial n} = 0 \tag{24}$$

where q' is the disturbance flow-variable and n is the unit vector normal to the boundary. The implicit nature of the compact differencing scheme can yield spurious reflections from the downstream boundary. Neumann conditions are employed for u', p' and ρ' at the bottom boundary AB, and $v' = 0$ is enforced for the vertical component of the disturbance to mimic the corresponding homogeneous boundary conditions of linear stability analysis as given in Eq. (22).

Fig. 4 shows contours of the vertical disturbance velocity component, v', for $A = 10^{-3}$ at $t = 1000$. At this time instant, the initial transient due to the onset of excitation at $t = 0$ convects out of the outflow boundary establishing a time harmonic disturbance field in the entire computational domain. Fig. 4 shows that of the three frequency cases considered, disturbances corresponding to $\omega = 0.145$ exhibit maximum growth, while those corresponding to $\omega = 0.0315$ and $\omega = 0.25$ exhibit near-neutral behavior. This agrees with the predictions of the linear inviscid instability theory. Likewise, the $\omega = 0.0315$ case displays perturbations with the largest wavelength (shortest wavenumber) while disturbances

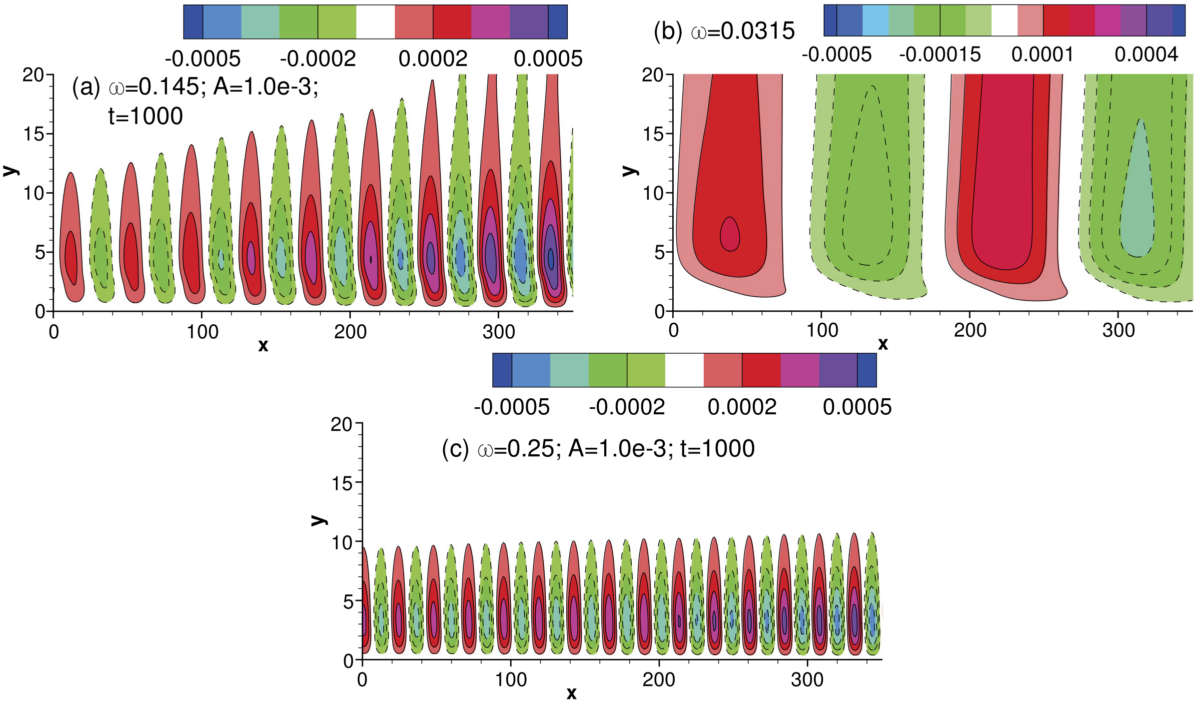

Fig. 4. Contours of v' plotted for (a) $\omega = 0.145$, (b) $\omega = 0.0315$ and (c) $\omega = 0.25$ at $t = 1000$. The amplitude of excitation is $A = 10^{-3}$. (For interpretation of the colors in the figure(s), the reader is referred to the web version of this article.)

corresponding to $\omega = 0.25$ have the shortest wavelength (largest wavenumber). These observations are consistent with the values listed in Table 1.

To further illustrate the characteristics of disturbance evolution, in Fig. 5, u' (frames (a), (b), (d) and (f)) and p' (frames (c), (e) and (g)) are plotted as functions of streamwise distance x at $y = 2.45$ for the indicated frequency cases. The amplitude of excitation is $A = 10^{-3}$ for all the cases shown. The transient evolution of disturbances is readily evident in u', Fig. 5(a). An approximate estimate of the speed of the front of the transient is 0.93, which is very close to the corresponding phase speed $c_r = 0.932$ for disturbances with $\omega = 0.145$ (see Table 1). Similarly obtained phase speeds corresponding to the other two frequency cases are also very close to their respective theoretical estimates. The wavenumber α_r of the disturbances can also be estimated from Figs. 5(b–g) for the corresponding frequency cases. For $\omega = 0.145$, this value from NS-MFP as shown in Figs. 5(b, c) is 0.15536, which approximates the predicted value of 0.15548 (see Table 1) very accurately. Similarly, estimated values of α_r for the other two non-optimal frequency cases (0.0345 for $\omega = 0.0315$ and 0.263 for $\omega = 0.0315$) from Figs. 5(d, e) and 5(f, g) are in very good agreement to those predicted by the theory (see Table 1).

Fig. 6 compares the streamwise variation of the normalized amplitude for disturbances as obtained from NS-MFP with those predicted from LST. Fig. 6 shows $A(x)/A(0)$ at a representative y-location of $y = 1.2$ for the optimal growth frequency $\omega = 0.145$ where, $A(x)$ and $A(0)$ indicate disturbance amplitudes at any given streamwise location x and at the inlet ($x = 0$), respectively. Frame (a) considers a low initial amplitude of $A = 1 \times 10^{-6}$, which ensures linear growth, while frame (b) considers a much higher value ($A = 10^{-2}$) to recover non-linear growth. According to the linear stability analysis, disturbance amplitudes should grow as $A(x) = A(x_0)e^{-\alpha_i(x-x_0)}$. For this optimal frequency, $\omega = 0.145$, the value of α_i is -0.2298×10^{-2} (see Table 1). Fig. 6(a) thus shows an excellent match of the x-variation of $A(x)/A(0)$ for all primitive variable fluctuations between LST and MFP, as expected. At higher amplitude, frame (b), significant deviations become evident, with density fluctuations displaying the most sensitive non-linear behavior.

The above entropy layer case verifies the theoretical discussion of Sec. 3 and Appendix A, when suitable conditions are applied on the basic state. The jet cases considered next are more challenging, since the basic state is derived by time-averaging LES or steady-state RANS. The time-averaged LES requires the forcing term to maintain constancy of the basic state. On the other hand for a RANS-derived base-flow, a similar forcing is only required if the eddy viscosity is neglected in the perturbation analysis, as discussed further in Section 5.3.

5. Application to jets

We consider free shear layers represented by jets at Mach 0.9 and 1.3 since these are representative of current interest to the community. Each case has an LES database, which has previously been confirmed to match near and far-field data (see [47] and [48,49] for the Mach 0.9 and 1.3 cases, respectively). For the Mach 0.9 jet case $T_{jet}/T_{amb} = 0.9227$, with $T_{jet} = 251$ K and $T_{amb} = 272$ K [47] while for Mach 1.3 jet $T_{jet}/T_{amb} = 0.7467$ with $T_{jet} = 224$ K and $T_{amb} = 300$ K [48]. Here, T_{jet} and T_{amb} indicate the temperatures of the jet at the nozzle exit plane and the surrounding ambient air, respectively. For each case, harmonic perturbations are introduced to obtain the modal response, whose qualitative and quantitative features are evaluated by considering results from the literature. To balance completeness and brevity, different approaches are employed to analyze the NS-MFP perturbations for the two cases. For the Mach 0.9 case, we compare to PSE results, similar to those employed by Ref. [27], while for the Mach 1.3 case, we use the original LES data. Likewise, we only focus on the near field, since the far-field extension may be obtained through wave propagator approaches such as those discussed in Ref. [8], and are not directly pertinent to the NS-MFP method. The mean flow for both cases is obtained by time-averaging the LES data, though for the Mach 1.3 case, a RANS-based result is also employed separately to examine issues related to eddy viscosity.

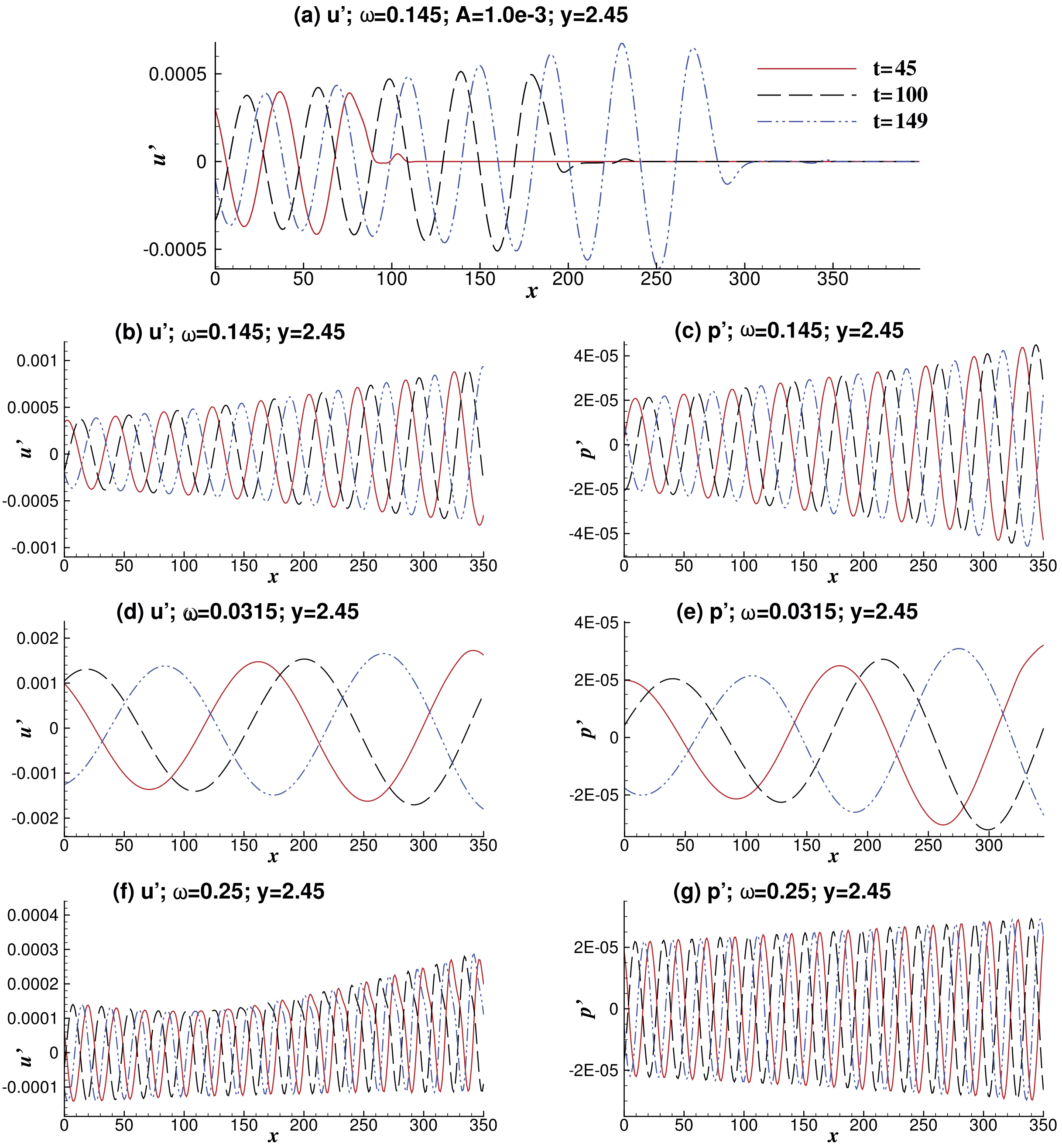

Fig. 5. u' (in frames (a), (b), (d) and (f)) and p' (in frames (c), (e) and (g)) plotted as a function of streamwise distance x for $y = 2.45$ and indicated frequency cases. The amplitude of excitation is $A = 10^{-3}$ for all the cases shown here. The time instants corresponding to disturbance plots shown in frames (b)–(g) are after the initial transient sweeps the entire computational domain.

5.1. *Mean flow perturbation of a Mach* 0.9 *turbulent round jet*

Fig. 7 highlights the general features of the unsteady flow with a Q-criterion [50] isosurface of the instantaneous turbulent flowfield, colored by streamwise velocity. The initial growth of fluctuations is dominated by the evolution of axisymmetric toroidal vortices due to Kelvin–Helmholtz like instabilities. The basic state, shown with streamwise velocity contours in Fig. 8, is obtained by averaging a validated LES in time as well as in the azimuthal direction. To focus on the shear layer, the evolution of perturbation is examined in the domain $x_0/D = 1.3433$ to $x_1/D = 31.30$ in the axial direction and $r_{max}/D = 17.66$ in the radial direction.

We first perform a qualitative assessment to show that the NS-MFP method generates similar disturbance field forms as with the PSE results documented in Ref. [27], and that the compact wave-packet structure is a common observation even when the forcing function differs in its details. A localized excitation in time is imposed on the basic state of Fig. 8 by considering a Gaussian function:

$$p'(x_0, r, t) = \alpha_1 \, f(r) \, \exp\left[-\left(\frac{t - t_0}{\sigma}\right)^2\right] \tag{25}$$

where $\alpha_1 = 0.05$ is the amplitude of excitation, $t_0 = 1$ is the time instant of the peak excitation and $\sigma = 0.1$ is the width of the Gaussian pulse. The excitation is also localized in the radial direction by specifying $f(r)$ as

$$f(r) = \frac{1}{2}\left[1 + \cos\left(\pi \frac{r - r_0}{\Delta r}\right)\right] \tag{26}$$

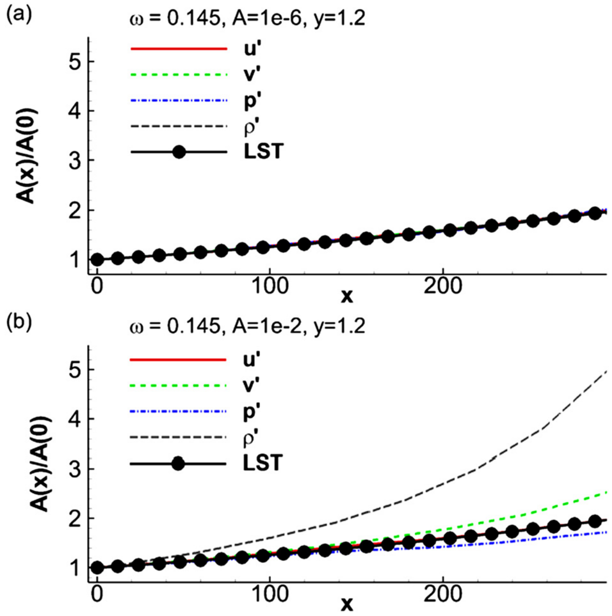

Fig. 6. $A(x)/A(0)$ plotted for u', v', p' and ρ' with LST results for (a) linear and (b) non-linear forcing at optimal frequency, $\omega = 0.145$. Here, $A(x)$ and $A(0)$ indicate disturbance amplitudes at any given streamwise location x and at the inlet ($x = 0$), respectively.

for $r_0 - \Delta r \le r \le r_0 + \Delta r$ and $f(r) = 0$, otherwise. Here $r_0 = 0.5D$ is the radial location of the lip-line and $\Delta r = 0.22D$ is chosen to ensure that the excitation is radially localized while containing sufficient number of grid points (in this case 10) to resolve the perturbation without numerical instability. Boundary conditions are similar to those employed for the stability analysis of axisymmetric flows in the literature [51,52]. Only the axisymmetric ($m = 0$) mode is employed – this can be justified by its superdirective dominance at low polar angles of interest [53,8]. Higher azimuthal modes can of course be incorporated through an appropriate function $g(\theta)$ in Eq. (25), where θ denotes the azimuthal angle, and considering the full 3-D flow-field. At the outflow and far-field of the computational domain, Neumann conditions are employed on the disturbance quantities, *i.e.*, u', v', w', p' and ρ'. At the centerline of the jet, u', p' and ρ' are specified by extrapolating from the interior, while v' and w' are specified to be zero. At the inflow, excitation is imposed by specifying perturbation pressure p' by Eq. (25) while the other four disturbance quantities are specified to be zero. Note that even when only pressure fluctuations are imposed, the response generates acoustic and entropic modes as well, since, for an ideal gas $dp = c^2 d\rho + (\gamma - 1)\rho T ds$, where c is the local speed of sound and dp, $d\rho$ and ds indicate changes in pressure, density and entropy, respectively. Vortical modes are also generated through the perturbation baroclinic term $(1/\rho_b^2)(\nabla\rho' \times \nabla p_b + \nabla\rho_b \times \nabla p')$ appearing in the corresponding disturbance vorticity transport equation, where the variables with subscript b refer to the base-flow quantities. The sixth-order compact scheme of Ref. [54] is used to discretize the inviscid flux. The fourth-order low storage Runge–Kutta time-integration scheme [46] is used with a time step of $\Delta t = 10^{-3}$. Long time integration is facilitated by artificially damping disturbances in a very narrow strip close to the outflow boundary.

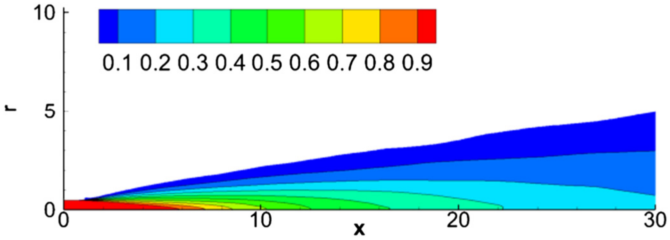

Fig. 8. Time and azimuthally averaged mean U-velocity contours of Mach 0.9 turbulent jet.

The spatio-temporal evolution of perturbation pressure (p') obtained by NS-MFP using the excitation of Eq. (25) is shown in Fig. 9 at the indicated time instants. The excitation clearly generates a downstream propagating wave-packet, which disperses as it moves downstream. A qualitative comparison may be obtained by considering the PSE-based results of Ref. [27], whose mean basic state is similar to that in Fig. 8, but was obtained from PIV data. The forcing function for the PSE analysis was comprised of temporally impulsive excitation at the inflow obtained by adding linear stability modes (with known eigenfunctions), corresponding to a range of Strouhal numbers ($St = fD/U_{jet}$) from 0.025 to 0.375 in steps of 0.025. These modes were then evolved with PSE for each frequency component and the spatio-temporal evolution of the perturbation at any instant was obtained by the inverse Fourier transform of the sum of the PSE solutions for each harmonic component in the spectral domain. The PSE results from Ref. [27] are shown in Fig. 10 at two representative time instants after the imposition of excitation. The primary feature is again a localized spatio-temporal wave-packet growing and propagating in

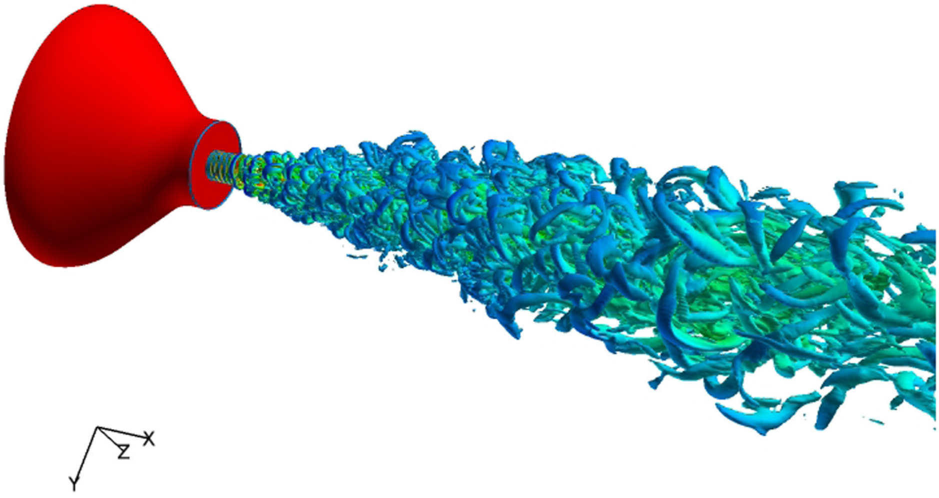

Fig. 7. Instantaneous $Q = 0.05$ isosurface of LES for Mach 0.9 jet ($Re = 635310$).

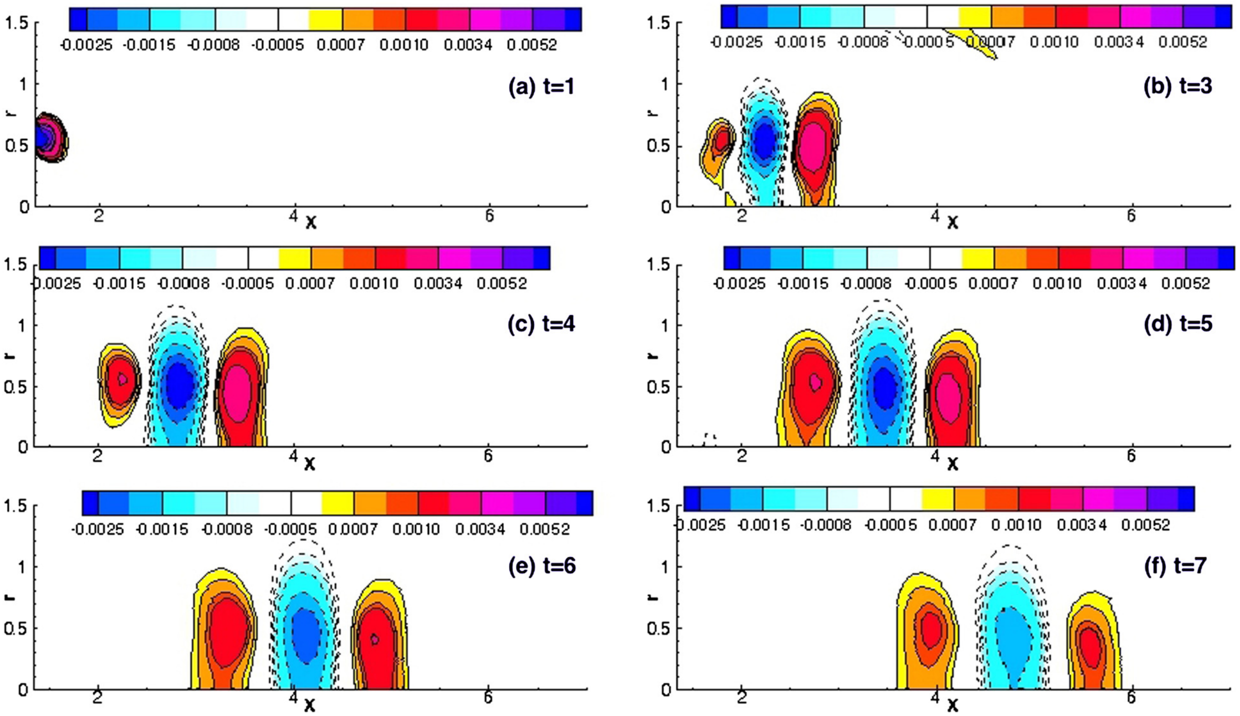

Fig. 9. Evolution of perturbation pressure p' for $M = 0.9$ jet plotted at representative time instants for the impulse response case computed via proposed mean flow perturbation method. The impulsive excitation at the inflow station is prescribed here by Eq. (25).

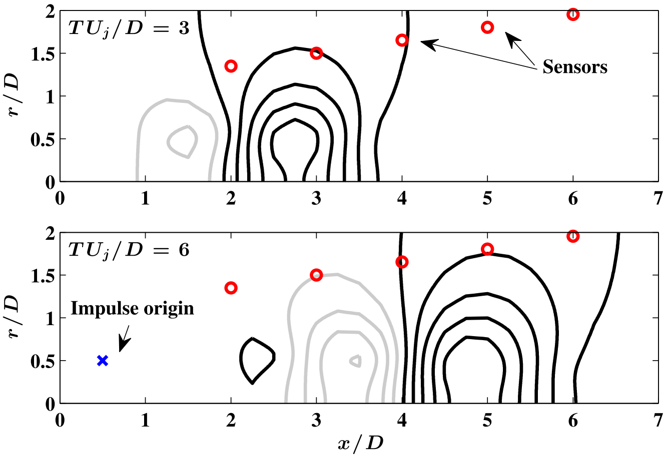

Fig. 10. Evolution of perturbation pressure p' for $M = 0.9$ jet plotted at representative time instants for the impulse response case as obtained by PSE.
Fig. 12 from Sinha et al. [27].

the downstream direction. As noted in Ref. [55], modulation and jittering of such wave-packets play a very crucial role in the acoustic emission due to the turbulent jet. Since the peak amplitude of the NS-MFP excitation is prescribed at $t_0 = 1$, the comparison with Fig. 10 can be accomplished by time-shifting the current results by $t = 1$. For example, frames (c) and (f) of Fig. 9 should be compared with the top and bottom frames of Fig. 10, respectively. The structures obtained with NS-MFP and PSE approaches are clearly qualitatively very similar, despite the differences in excitation details as well as the mean flow.

For a more quantitative comparison, we consider the response to one specific frequency, using the same excitation and basic state for both PSE as well as NS-MFP. The excitation corresponds to the axisymmetric $m = 0$ mode at a Strouhal number of 0.3, while the basic state is the computationally derived solution depicted in Fig. 8, truncated to $2 \le x/D \le 10$ and $0 \le r/D \le 5$ along streamwise and radial directions respectively. At the starting PSE solution location ($x/D = 2$), the mode shape functions and the complex wavenumber are chosen from the local linear stability analysis of the corresponding jet-profile for $St = 0.3$. These shapes for horizontal and radial velocity components at $x/D = 2$ for $St = 0.3$ are shown in frames (a) and (b) of Fig. 11, respectively. The corresponding mode-shapes for perturbation pressure and density are shown in frames (c) and (d) of Fig. 11, where subscripts r and i refer to the real and imaginary parts of each complex eigenfunction. Since only the axisymmetric mode is considered here, the mode shape function for the disturbance azimuthal component of velocity is identically zero. 400 points are used in the radial direction, clustered near the centerline of the jet to achieve adequate resolution.

The same excitation function is imposed as in the PSE method by specifying the mode shape functions at the inlet of the computational domain ($x/D = 2.0$), similar to that given in Eq. (23). The evolution of disturbances with NS-MFP is shown in Fig. 12 with contours of u' velocity in the (x, r)-plane at the indicated time instants. The amplitude of excitation is $A = 10^{-6}$, which is small enough to ensure linear evolution of disturbances. The progressive spatio-temporal development of a time-harmonic wave solution in the entire computational domain is evident, as is the spatial growth of disturbances. Fig. 12 also reveals that the wavenumber of the time-harmonic perturbation increases as it moves downstream. This observation is consistent with the PSE analysis and other corresponding stability results.

We preface the direct comparison by noting that the two approaches have very different assumptions, which must be taken into account. In addition to the slow streamwise variation assumption, PSE also encounters the problem of residual ellipticity from streamwise pressure gradients and streamwise diffusion terms, as detailed in Refs. [56,6,57,7]. To damp modes associated with residual ellipticity, PSE imposes a minimum streamwise step size, which also has the effect of reducing streamwise gradients. In the

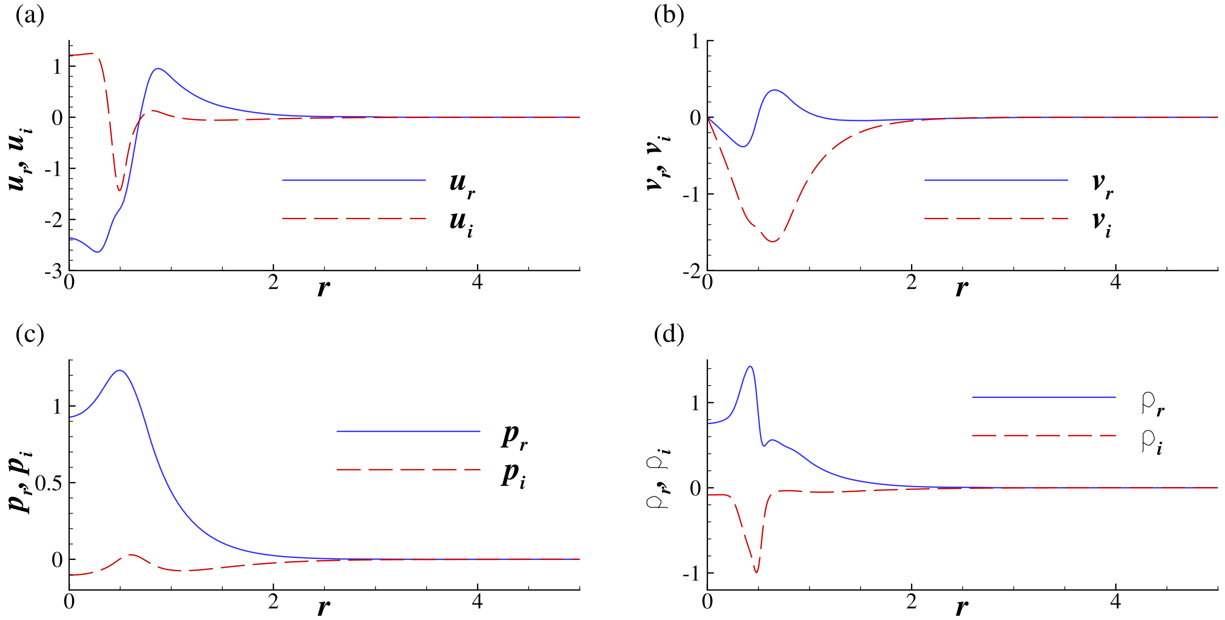

Fig. 11. Real and imaginary part of the complex mode-shape functions shown for (a) u', (b) v', (c) p' and (d) ρ' at $x/D = 2$.

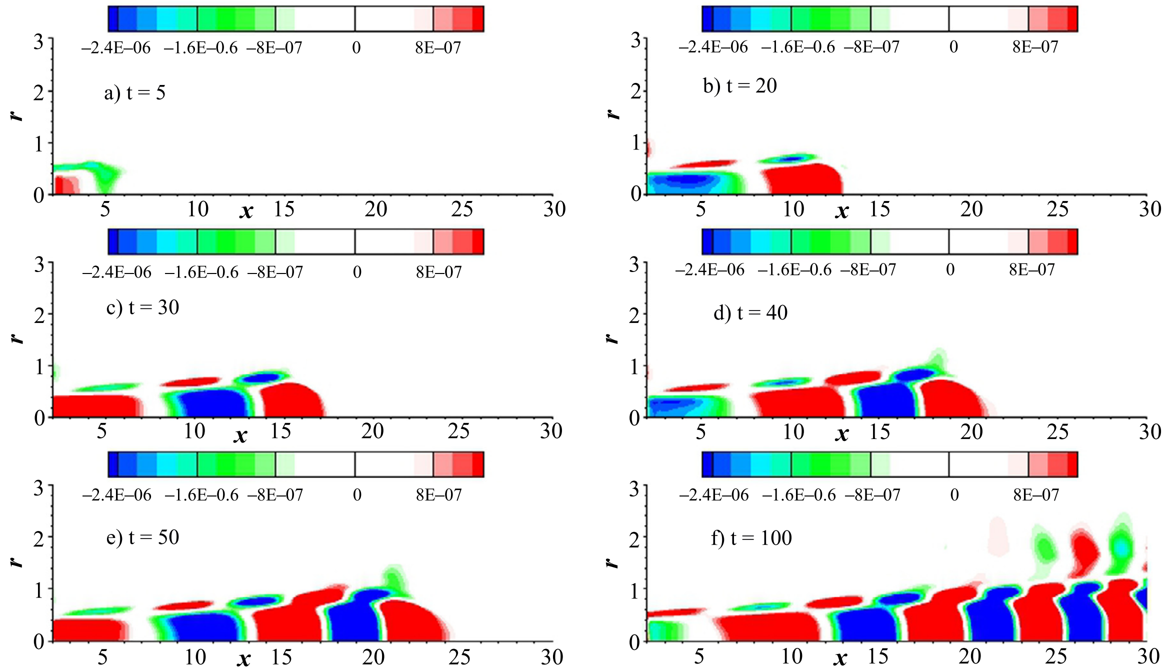

Fig. 12. Contours of u' plotted in (x,r)-plane at indicated time-instants when the mean flow shown in Fig. 8 is excited at $x/D = 2$ by LST mode-shape functions (Fig. 11) for $St = 0.3$ and $m = 0$.

present case, the computational mesh for PSE was coarsened along the streamwise direction by considering only 24 uniformly spaced grid-points. Such a coarse streamwise grid is however unsuitable for the NS-MFP approach, since it leads to a large truncation error. Therefore, a fair comparison with PSE requires reduction of the streamwise variation of the basic state for NS-MFP, without compromising the fineness of the mesh required to reduce discretization error.

To accomplish this, we note that PSE disturbances are expressed as:

$$\mathbf{q}'(x,r,\phi,t) = \widetilde{\mathbf{q}}(X,r)\ \exp\left[i\left(\int_{\bar{\xi}} \alpha(\bar{\xi})d\bar{\xi} + m\phi - \omega t \right) \right] \tag{27}$$

where $X = \epsilon x$, $\epsilon \ll 1$ and m is an integer. The streamwise variation of the base-flow is thus constrained to be slow through ϵ, together with the assumption that the second derivatives of perturbation mode shape functions $\widetilde{\mathbf{q}}$ are sufficiently small to be neglected. For NS-MFP therefore, streamwise derivatives can be reduced by simply applying a stretch factor to the NS-MFP basic state mesh, without altering the crucial transverse variation. The bounds of mesh stretching can be obtained by examining the rate of change on the PSE and NS-MFP meshes. The region $2 \le x/D \le 10$ is effectively discretized with 24 points for PSE, whereas NS-MFP uses 240 points in the same region. For illustration, a second order $\partial u/\partial x$ numerically by a second-order approximation for PSE corresponds

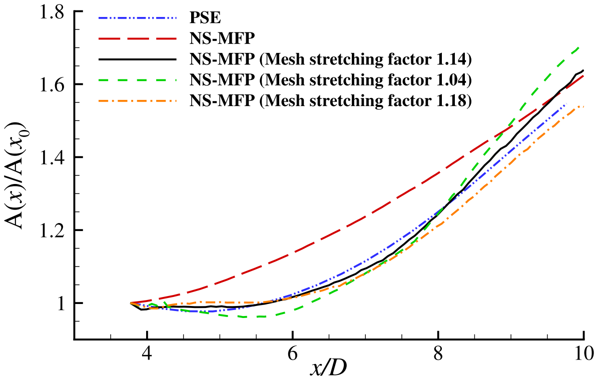

Fig. 13. Streamwise variation of $A(x)/A(x_0)$ plotted for indicated cases, where $A(x)$ and $A(x_0)$ are the amplitudes of u'_{max} at streamwise stations x and x_0, respectively.

to

$$\left[\frac{\partial u_i}{\partial x}\right]_{PSE} = \frac{u_{i+10} - u_{i-10}}{20\Delta x}$$

while the same quantity would be evaluated as

$$\left[\frac{\partial u_i}{\partial x}\right]_{NS-MFP} = \frac{u_{i+1} - u_{i-1}}{2\Delta x}$$

in NS-MFP. Thus, to match axial gradients, a local grid stretch factor of approximately $\hat{F} = \left([u_{x_i}]_{NS-MFP}/[u_{x_i}]_{PSE}\right)$ is required. In effect, we stretch our computational domain by $\hat{F}$ along x-direction, thereby increasing the average streamwise grid-spacings by this factor. This effectively reduces the streamwise gradients to values similar to those in the PSE, while maintaining a mesh density suitable for the finite-difference technique. The factor $\hat{F}$ can be estimated *a priori*, but naturally varies with streamwise distance, since the basic state gradients are not constant. For $4.2 \le x/D \le 7.6$, $\hat{F}$ varies from 1.2 to 1.1, with an average value of approximately 1.14.

Results are shown for various simulated cases in Fig. 13. Here $A(x)/A(x_0)$ is plotted as a function of x/D, where $A(x)$ and $A(x_0)$ are the amplitudes of u'_{max} at streamwise stations x and x_0, respectively. u'_{max} is the maximum of $|u'|$ over all radial locations and the ariation of normalized amplitude corresponding to PSE is computed by numerically integrating $-\alpha_i$ from x_0 to x, *i.e.*,

$$\left[\frac{A(x)}{A(x_0)}\right]_{PSE} = \exp\left(\int_{x_0}^{x} (-\alpha_i)\, dx\right)$$

The naive comparison (marked NS-MFP), uses the basic state without any modification. The initial growth is substantially higher than that obtained with PSE. The results are consistent with the discussion above: the NS-MFP method accounts for the correct (large) initial gradients in the basic state, leading to the observed high growth rate. Results with several $\hat{F}$ values are also shown on Fig. 13. Satisfactory agreement is clearly achieved if $\hat{F}$ lies between 1.14 and 1.18. The value 1.14 yields the best average match with PSE growth rate over $3.77 \le x/D \le 10$. At the downstream end of the domain however, the NS-MFP rate asymptotes to a higher value than with PSE. This is a consequence of the fact that a single stretch factor value cannot account for the spatially changing gradients in the basic state. Moreover, since the comparison of MFP results with PSE requires modification of the basic state to reflect PSE constraints, these are necessarily dependent on the domain of interest. In principle, a variable stretch factor based on local streamwise gradients could ensure a better match, but the exercise does not provide much new insight. In summary therefore, the conditions required in Appendix A can only be satisfied when similar constraints as required for PSE are also enforced on the base-flow for NS-MFP.

5.2. NS-MFP analysis of Mach 1.3 perfectly-expanded jet

We now consider the supersonic jet, and use suitably filtered results from the LES as the truth model to analyze the performance of NS-MFP. As noted earlier, the database, described in Ref. [49,58], has been employed in several studies [59]. Fig. 14 shows representative aspects of the flow after statistical stationarity has been achieved with azimuthal vorticity and dilatation ($\nabla \cdot \vec{V}$) in frames (a) and (b), respectively. The shear layer breaks down at the lip-line slightly downstream of the nozzle exit, where the boundary layer has been assumed to be laminar. The resulting structures are initially azimuthally coherent and roll-up to form vortices. These structures subsequently, entrain fluid and the disturbed flow increasingly penetrates towards the axis. Further downstream, the turbulent flow is dominated by coherent vortical structures which play an important role in the energy-cascade to the fine-scale eddies, and have major influence on the noise field. The dilatation contours of frame (b) are a surrogate for the sound field outside of the turbulent regions of the jet. The dominant acoustic radiation direction is at shallow angles, due to Mach wave radiation associated with the large turbulent structures moving at a supersonic group velocity (see *e.g.*, Ref. [60]). By contrast, radiation is less prominent along upstream or higher polar angles, which are due to the fine-scale turbulence [60]. Further details of the near field are discussed below.

Key features of the basic state employed are plotted in Fig. 15, which show mean U-velocity and pressure P contours. As before, this field is obtained through time- and azimuthally-averaging the turbulent field. The overall features are generally similar to those of the Mach 0.9 jet discussed above. This basic state is perturbed by once again imposing a pressure perturbation, p', at the nozzle exit plane close to the lip-line:

$$p'(x,r,t) = \alpha_m\, \sigma(x,r)\, \mathcal{R}(e^{2i\pi St\, t}) \tag{28}$$

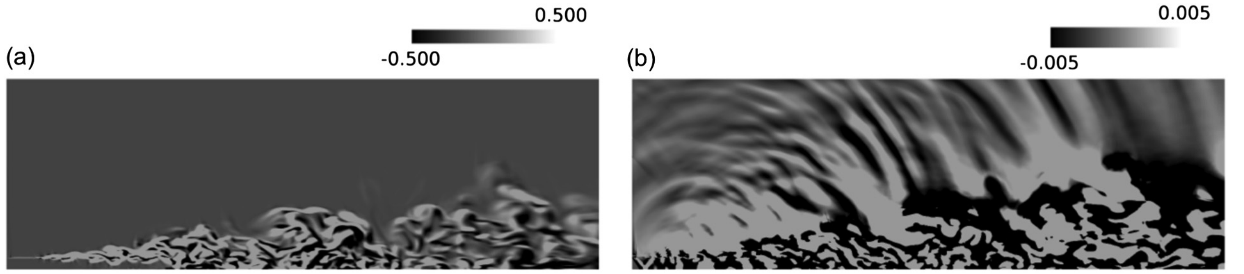

Fig. 14. Instantaneous snapshots of azimuthal vorticity ω_θ and velocity-divergence $\nabla \cdot \vec{V}$ of turbulent Mach 1.3 perfectly-expanded jet after reaching statistical-stationarity are plotted at a radial-plane in frames (a) and (b), respectively.

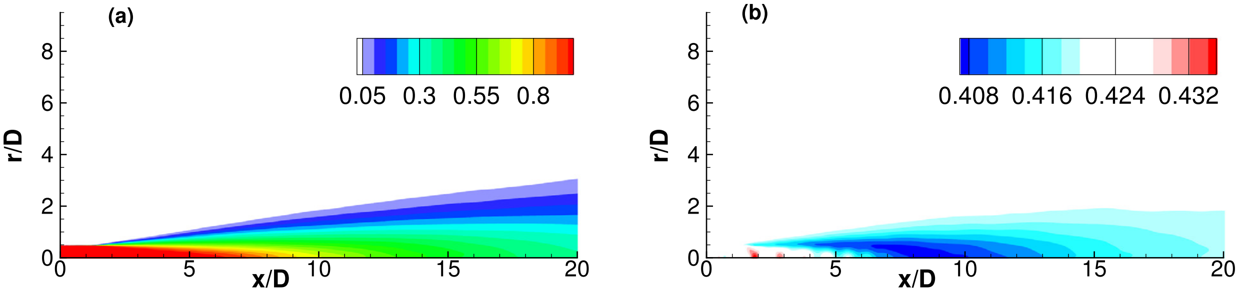

Fig. 15. (a, b) Contours of U-velocity and pressure P of the axisymmetric basic-state obtained by time- and azimuthally-averaging statistical stationary turbulent Mach 1.3 flow.

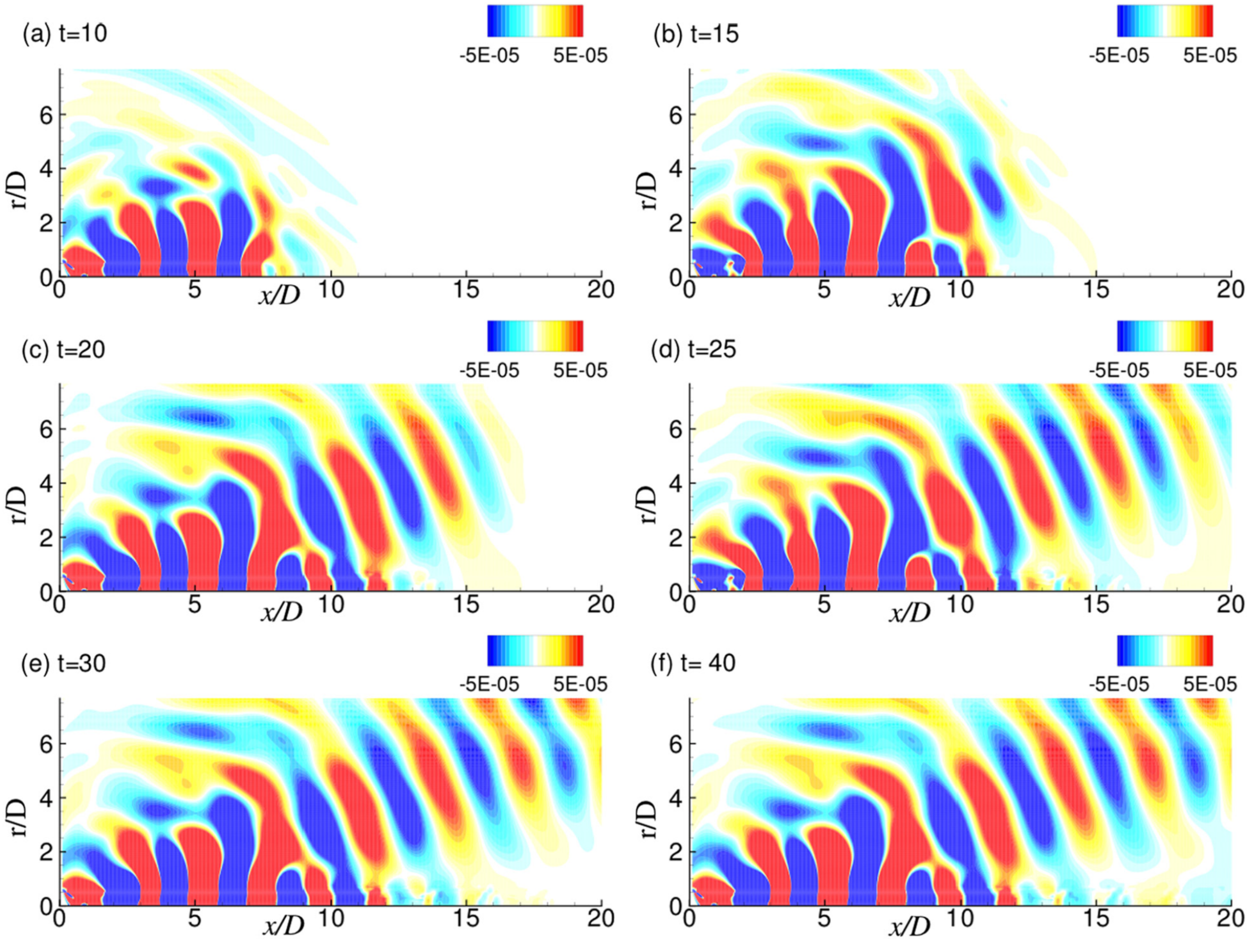

Fig. 16. Evolution of disturbance pressure p' corresponding to excitation Strouhal number of $St = 0.3$ plotted in the (x, r)-plane at (a) $t = 10$, (b) $t = 15$, (c) $t = 20$, (d) $t = 25$, (e) $t = 30$ and (f) $t = 40$ for Mach 1.3 perfectly-expanded jet case.

where $\mathcal{R}(\cdot)$ denotes the real part of the complex quantity enclosed within the parenthesis, St and α_m indicate the Strouhal number and the amplitude of the imposed excitation. In Eq. (28), $\sigma(x, r)$ represents a Gaussian-like function which is localized close to the lip-line. The maximum value of $\sigma(x, r)$ is unity and $\alpha_m = 10^{-4}$, to ensure that the disturbances remain in the linear regime.

In Fig. 16, the evolution of disturbance pressure p' corresponding to excitation Strouhal number of $St = 0.3$ is plotted in the (x, r)-plane at the indicated time instants. The initial transient response dies down beyond $t \sim 25$, and a time-harmonic solution is obtained. Two distinct components are evident from the disturbance contours. Close to the jet centerline, a clear wave-packet (or “wave-guide”) like behavior [61–63] is observed whose amplitude initially grows and attains maxima around $x/D \simeq 6.25$, before decaying. This wave-packet is associated with the corresponding instability waves for this particular Strouhal number. Away from the turbulent jet region, the disturbance takes a distinctively acoustic wave propagation character, essentially radiation associated with the wave-packet, which is confined close to the jet-centerline.

The wave packet form of the perturbation is consistent with the discussion in Sec. 1, regarding the influence of its evolution and propagation as a source of coherent sound radiation by turbulent jets [24,26,64]. Like the behavior in Fig. 16, such wave-packets display growth, saturation and decay of amplitudes whose spatial extent is significantly larger than the turbulence length scales [61]. While the fluctuation energy corresponding to these non-compact wave-packets is considerably lower than the compact and stochastic turbulent eddies, these are more acoustically efficient than the latter sources of noise radiation [55,61,59]. Fig. 16

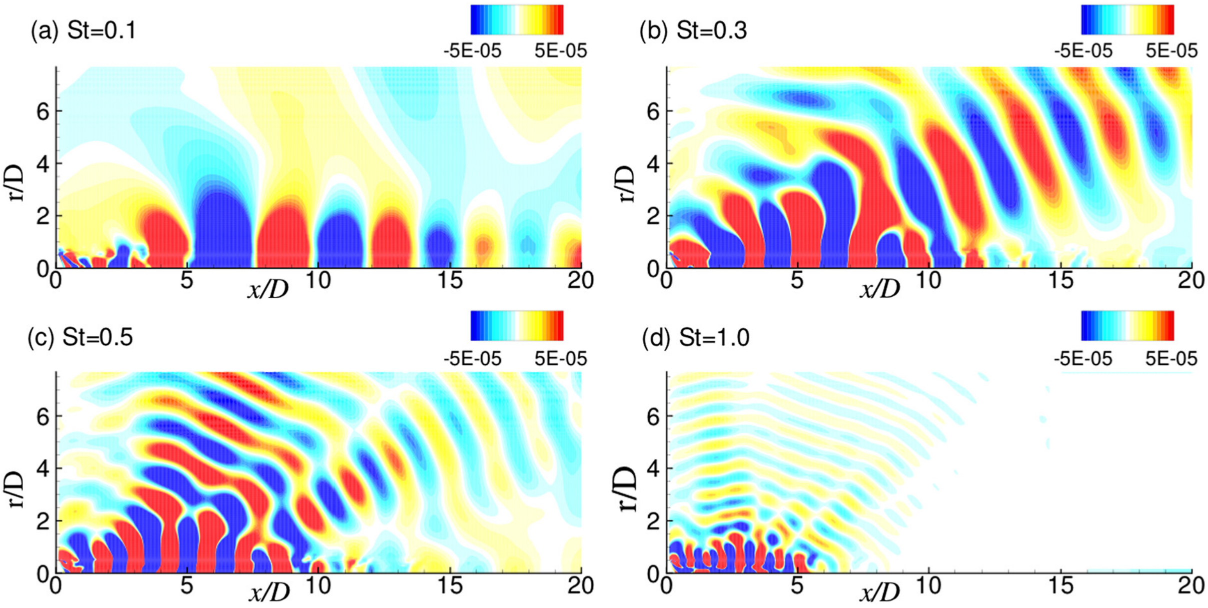

Fig. 17. Contours of time-harmonic disturbance pressure p' corresponding to indicated excitation Strouhal number plotted in the (x, r)-plane.

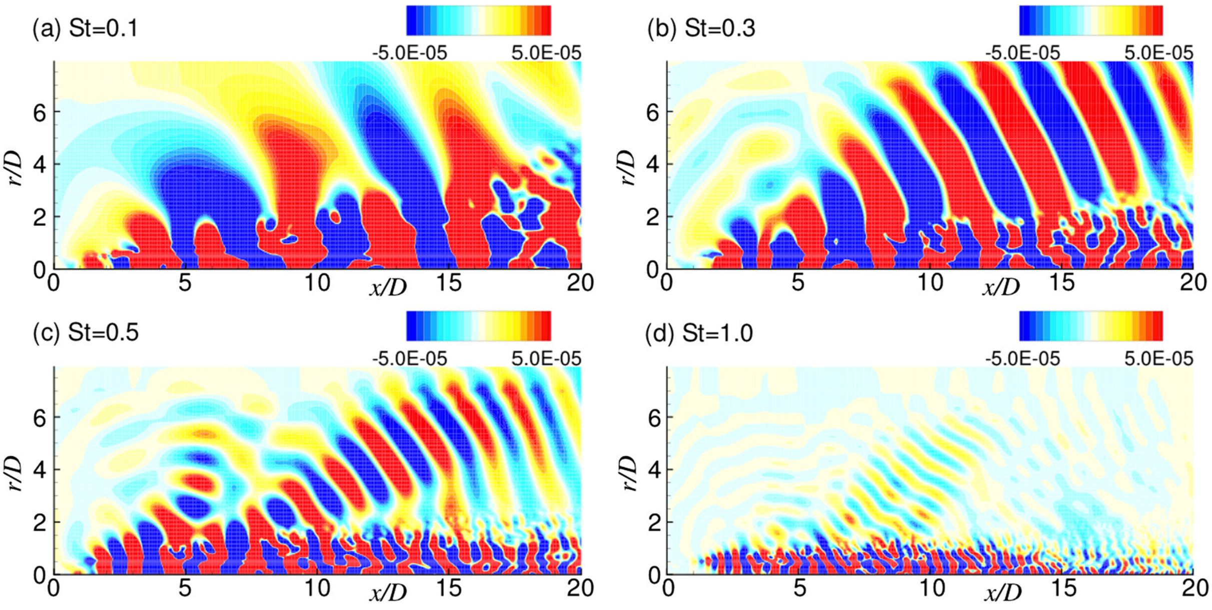

Fig. 18. Contours of time-harmonic disturbance pressure p' obtained from the actual full LES of the turbulent Mach 1.3 jet plotted in the (x, r)-plane for corresponding indicated Strouhal number.

suggests that the present NS-MFP approach can successfully capture and predict some of the important features of the linear wave-packet and sound radiated by these coherent sources. Moreover, as the amplitude of excitation is very low, the generated wave-packet is predominantly in the linear regime. Linearity of the response also implies that the NS-MFP approach is unable to simulate the influence of compact turbulent eddies. Therefore, this method cannot predict the noise generated by fine-scale turbulence, which primarily influences sound radiation along side-line directions [65].

Fig. 17 plots the statistically stationary time-harmonic disturbance pressure p' after the initial transient convects out of the domain, for Strouhal numbers of 0.1, 0.3, 0.5 and 1.0 in frames (a–d), respectively. Fig. 17(a) shows that disturbances corresponding to $St = 0.1$ display acoustic radiation of lower intensity and the field is confined to the jet-centerline with a maximum amplitude occurring around $x \simeq 6.8$, after which the amplitude decays. The $St = 0.3$ component has been discussed earlier in the context of Fig. 16 which reiterates the existence of the wave-packet component in the core of the jet, and the acoustic radiation in the near acoustic field, predominantly between polar angles of 17° and 40°, with respect to the center of the nozzle exit plane. At the higher frequency of $St = 0.5$, these two features are also evident, but the wave-packet is smaller and achieves a maximum nearer the nozzle exit plane. The radiated noise is lower than for $St = 0.3$ and is spread over a larger range of polar angles (between 30° and 105° with respect to the center of the nozzle exit plane). This trend continues as the excitation frequency is increased to $St = 1.0$ as shown in Fig. 17(d).

The results from the NS-MFP procedure are now assessed by comparison with the LES database. Fig. 18 shows contours of disturbance pressure p' for the indicated Strouhal numbers obtained

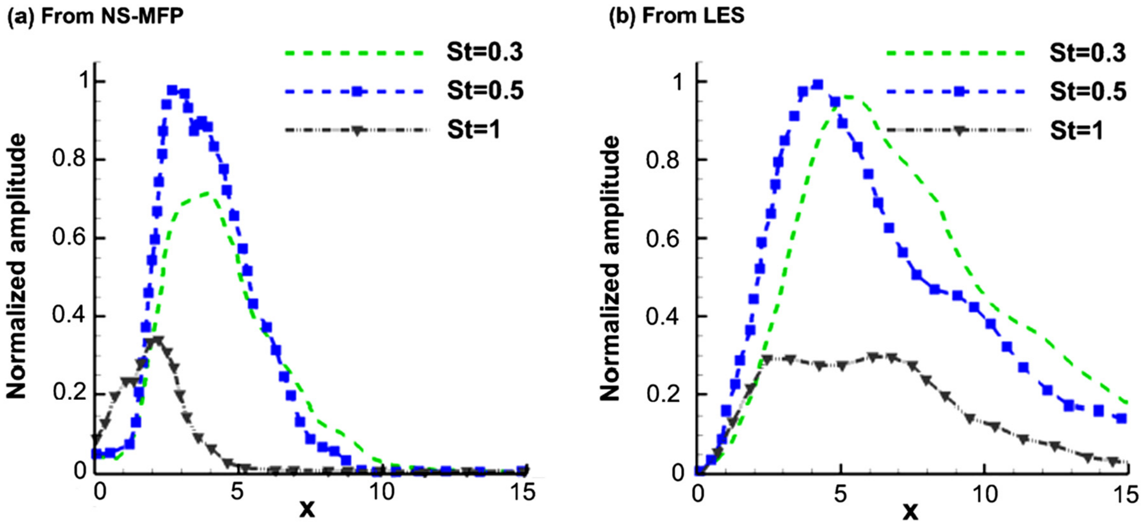

Fig. 19. (a, b) Axial variation of the normalized amplitude of disturbance pressure p' at the lip-line plotted for indicated Strouhal numbers for NS-MFP and time-accurate implicit LES, respectively.

from the actual LES of the turbulent Mach 1.3 jet. Note that no perturbations are explicitly imposed on the LES to induce breakdown. The shear layer exiting the nozzle is very unstable, and numerically introduced perturbations are sufficient. After the flow has reached a statistically stationary state, instantaneous fluctuations are obtained by subtracting the time-averaged flow from the instantaneous state. The axisymmetric azimuthal mode, $m = 0$, of these instantaneous fluctuations are then extracted by azimuthally averaging the perturbations. For $m = 0$ mode, the disturbance quantities at each St are obtained by first performing a Fast Fourier Transform (FFT) of the time-series of the perturbation data at each grid-location and subsequently reconstructing the data by inverse FFT. As anticipated, Fig. 18 shows that the LES results also display strong directivity of the noise-radiation based on the Strouhal number. The qualitative similarity between NS-MFP and LES for the dominant $St = 0.3$ form is also evident, and is consistent with Mach-wave radiation of disturbances associated with the part of the underlying wave-packet which travels at a supersonic group-velocity [64,65], as well as the wave-packet model of the supersonic jet-noise [8]. Note that sideline radiation does not prominently appear in Fig. 18, since only the $m = 0$ mode has been filtered out of the LES solution. Although the comparison between dominant features of LES and NS-MFP is good, discrepancies are evident with respect to the lower, $St = 0.1$ component, possible reasons for which are discussed later.

Fig. 19 displays the axial variation of the normalized amplitude of disturbance pressure p' at the lip-line for various Strouhal numbers. Since the amplitudes of the imposed perturbations are small, the disturbances evolve linearly. This indicates that the absolute values of the amplitude itself are not important, but the trends are. This is the motivation behind comparing the normalized amplitude of p' for different Strouhal numbers. The amplitudes in Fig. 19(a) and (b) are normalized with respect to the corresponding maximum amplitude *i.e.* the amplitude at $St = 0.5$. For the corresponding dominant components *i.e.*, $St = 0.3$ and 0.5, agreement on the approximate locations of the peaks and the trend of the streamwise variation of the corresponding amplitude profiles are noted. The mismatch in amplitudes at the high ($St = 1.0$) frequency is consistent with the contour plots of Fig. 17 and is associated with fine-scale turbulence, not considered in the mean flow analysis. Overall, the results agree with the postulate that the mean flow perturbation yields insight into the dominant relatively large scale features arising from mean flow instabilities.

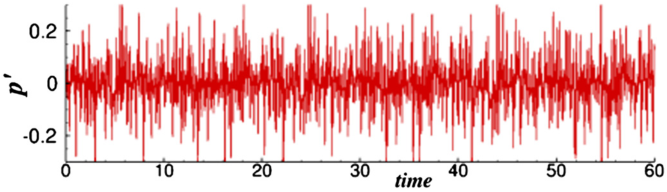

Fig. 20. Time variation of the imposed disturbance pressure at the exciter location for multi-periodic excitation case.

To further examine the performance of NS-MFP approach in predicting key elements of the acoustic field, we replace the monochromatic excitation with a multi-frequency input. The imposed localized disturbance pressure for this case is given as

$$p'(x, r, t) = \alpha_m \sigma(x, r) \sum_{n=1}^{N} \mathcal{R}(e^{i(2\pi St_n t + \phi_n)}) \tag{29}$$

where St_n and ϕ_n are the excitation Strouhal number and phase difference of the nth frequency component, while $\alpha_m = 10^{-4}$ is the excitation amplitude. The phase difference ϕ_n is chosen such that it varies randomly between 0 and 2π. Altogether, 191 different frequencies are used linearly spanning the range $0.1 < St < 2.0$. The corresponding time variation, mimicking white noise excitation, is shown plotted in Fig. 20.

To quantitatively compare the PSD obtained from NS-MFP and LES data-set, in Fig. 21 we plot normalized PSD of p' at the indicated polar angles (calculated with respect to the center of the nozzle exit plane and at a distance of $12D$ from it). The red solid-lines in this figure correspond to the results obtained from NS-MFP while the black dotted lines are from the $m = 0$ mode of the LES data-set. The PSD is normalized with respect to its corresponding maximum value. This figure shows good match for the fall of the spectra at moderately high Strouhal numbers, particularly at $\theta = 40°$ and $60°$. High-frequency spectra associated with fine scale turbulence are not reproducible by NS-MFP, since those sources are absent in the basic state. The performance degradation at lower Strouhal numbers for the axisymmetric mode is similar to that reported in Ref. [8]. White-noise excitation, as examined here, specifies that all the frequency-components have equal amplitudes, which does not represent a real-life scenario. The actual response will depend on the relative amplitude and radial variation of various frequency components in the incoming flow. This is a likely

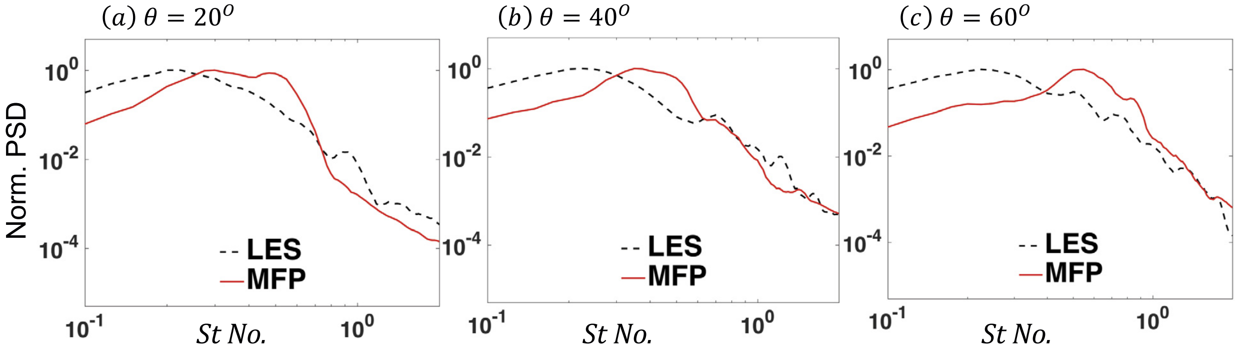

Fig. 21. Normalized power spectral density of disturbance pressure p' as obtained from NS-MFP and LES plotted for indicated polar angles (θ). The polar angle θ is calculated with respect to the center of the nozzle exit plane at a distance of $12D$ from it. The red-lines correspond to the results obtained from NS-MFP while the black dotted lines are from the $m = 0$ mode of the LES data-set.

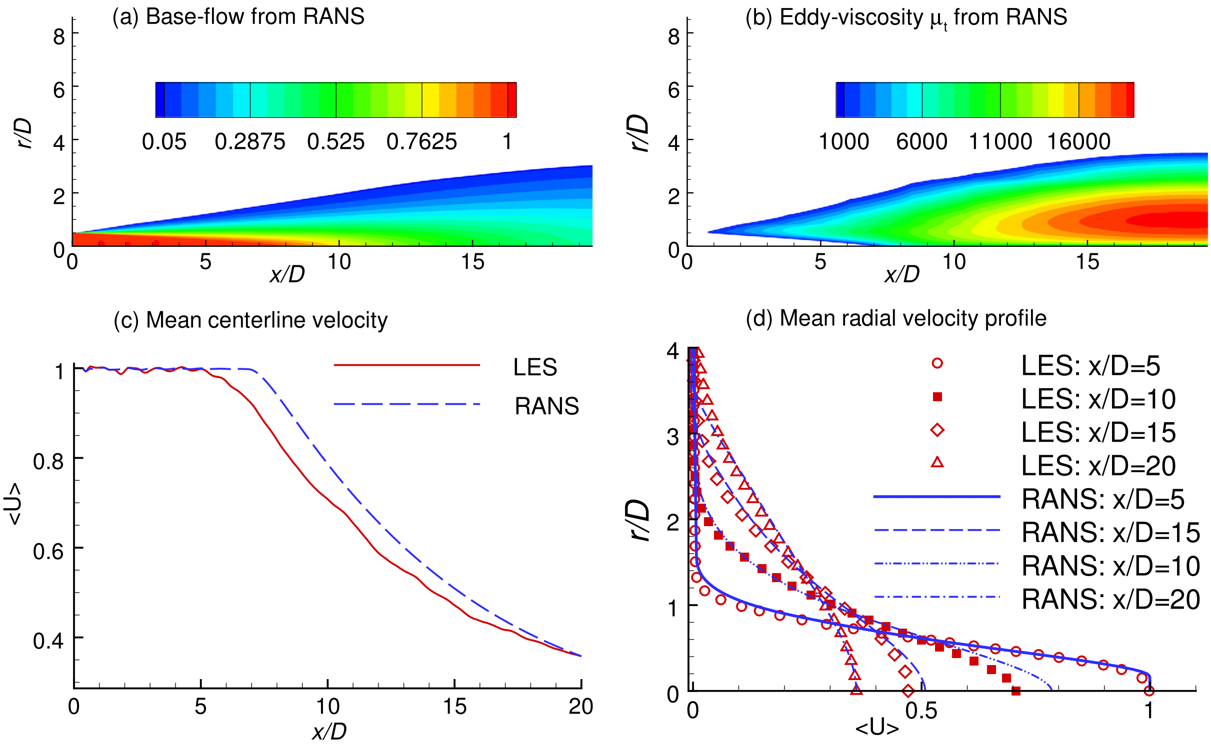

Fig. 22. Contours of (a) the base-flow obtained from RANS and (b) eddy-viscosity μ_t plotted in (x, r)-plane. (c) Axial variation of the centerline velocity and (d) radial variation of the horizontal velocity component plotted for base-flows corresponding to RANS and mean of LES.

reason for the mismatch of the axial variation of the amplitudes for the low-frequency components. In [66], LES data was projected onto the relevant families of instability waves by bi-orthogonal decomposition to obtain appropriate inlet conditions (including the amplitude and shape functions) to educe near-field pressure fields for PSE analysis of Mach 1.5 supersonic jet. Therefore, we speculate that NS-MFP with a frequency dependent amplitude variation of excitation Strouhal numbers at the nozzle-exit, obtained from either LES or experiments might show a better match in terms of the spectral content at lower Strouhal numbers.

5.3. *Use of RANS-based mean flow-field for Mach* 1.3 *perfectly-expanded jet*

The above analysis used a basic state derived by time-averaging LES. A major advantage accrues if this basic state is obtained from RANS, since such solutions are far cheaper to obtain. In this section, we examine the issues related to the use of RANS-derived basic states, most importantly on the treatment of eddy viscosity, again focusing on the Mach 1.3 case.

The $(k - \epsilon)$ turbulence model [67] with compressibility correction are used, as implemented in Ref. [68]. Fig. 22(a) shows the base-flow, with contours of the horizontal velocity component plotted from 0.05 to 1.0 at intervals of 0.0475. Comparing this RANS result with the corresponding LES field (Fig. 15(a)), there is overall similarity in the features, but the shear-layer grows more rapidly than that of the LES. Fig. 22(b) shows the eddy viscosity field (μ_t), which is mostly confined in the shear-layer and is maximum around $x/D \simeq 20$. However, this does not correspond to high Reynolds stresses, since local gradients are relatively small. Fig. 22(c) compares the axial variation of the mean centerline velocity for base-flows from LES and RANS – the latter has a slightly more elongated core region and a modestly higher subsequent decay. Fig. 22(d) compares streamwise velocity versus radial distance at several streamwise locations ($x/D = 5$, 10, 15 and 20). Except for a small region close to the jet-centerline, both approaches display very good quantitative match.

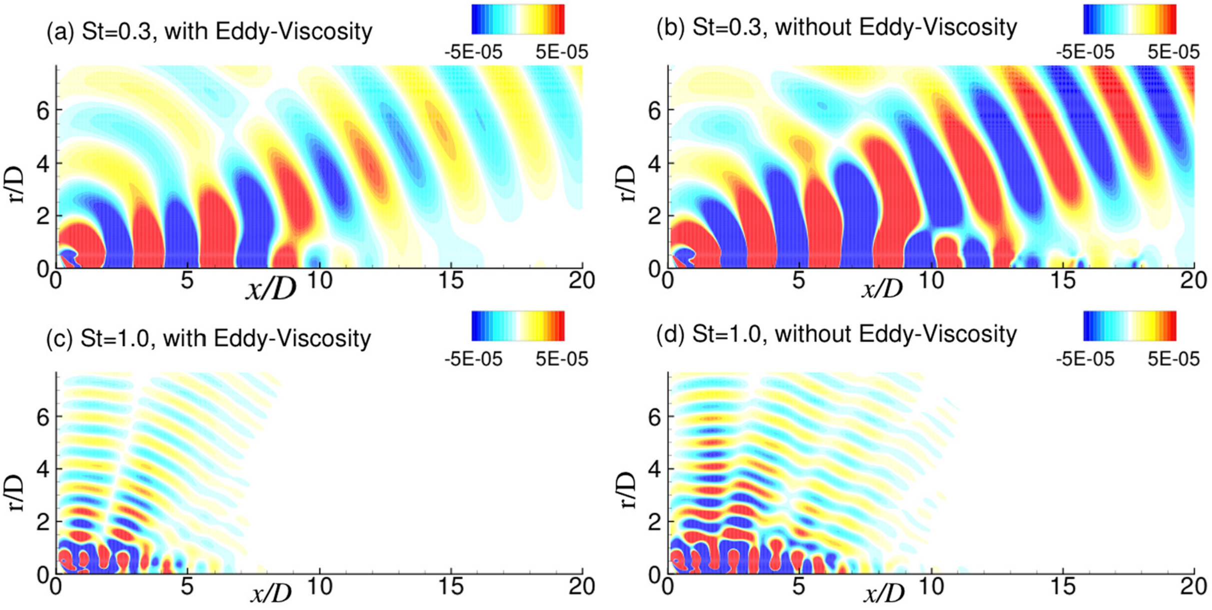

Fig. 23. Contours of time-harmonic disturbance pressure p' corresponding to (a, b) $St = 0.3$ and (c, d) $St = 1.0$ plotted in the (x, r)-plane when RANS based base-flow is used for NS-MFP. Frames (a) and (c) corresponds to the cases where eddy-viscosity μ_t is included for NS-MFP while frames (b) and (d) are for the cases when μ_t is excluded for NS-MFP.

Although this would suggest that the NS-MFP results should behave similarly with both profiles, an important question arises on the treatment of eddy viscosity. We consider this in the context of the triple decomposition approach of Reynolds and Hussain [69]:

$$Q(\vec{X},t)=\overline{Q}(\vec{X})+\widetilde{Q}(\vec{X},\epsilon t)+Q''(\vec{X},t) \tag{30}$$

where $\overline{Q}(\vec{X})$ is the time-invariant mean flow, $\widetilde{Q}(\vec{X},\epsilon t)$ represent low-frequency large-scale coherent structures and $Q''(\vec{X},t)$ denote incoherent/random fluctuations. While $\overline{Q}$ can be obtained from RANS-like approaches (the only difference being the presence of a term which specifies the extraction of energy from the mean flow to the organized structures), the evolution of $\widetilde{Q}$ is given as:

$$\frac{\partial\widetilde{Q}}{\partial t}=\mathcal{L}(\overline{Q},\widetilde{Q})+\mathcal{N}(\overline{Q},\widetilde{Q})-\tilde{r} \tag{31}$$

where $\mathcal{L}()$ and $\mathcal{N}()$ denote linear and non-linear operators, respectively. The ith-component of the vector $\tilde{r}$ for an in compressible flow is given as:

$$\tilde{r}_i=\frac{\partial}{\partial x_j}\left(\langle u_i'u_j'\rangle-\overline{u_i'u_j'}\right) \tag{32}$$

Here, $\langle\cdot\rangle$ denotes phase-averaging, $\bar{\cdot}$ denotes time-averaging and u_i' represents fluctuating velocity components. Essentially, the term $\tilde{r}$ represents a sink signifying drain of energy from large-scale structures due to its interactions with incoherent fluctuations. Reynolds and Hussain [69] and several other researchers (e.g. Lifshitz et al. [70]) have pointed out the need to model this term correctly to capture the dynamics of the coherent structures so that the interactions between the high-frequency random fluctuations and low-frequency coherent structures are accounted for. Lifshitz et al. [70] also note that use of an inaccurate model for turbulence-coherent interactions can lead to an erroneous prediction of the evolution and propagation of large-scale coherent structures. Note that though Eqs. (30)–(32) are valid for incompressible flows, similar considerations hold for the compressible scenario. On the contrary, there also exists an alternative view-point that the effect of the inherent nonlinearities and turbulence-coherent interactions of the flow is implicitly incorporated in the mean turbulent flowfield insofar as the characteristics of the large-scale structures are concerned [26]. Numerous efforts, including Refs. [21,71,26,72,73] therefore, do not explicitly consider the eddy viscosity in the analysis. To address this issue, we present and compare two sets of simulation results in the present section while using base-flow obtained from RANS for NS-MFP. In the first set, eddy-viscosity μ_t terms are included and in the second set these are excluded – note that in the latter case, the term $\tilde{r}$ of Eq. (31) is zero.

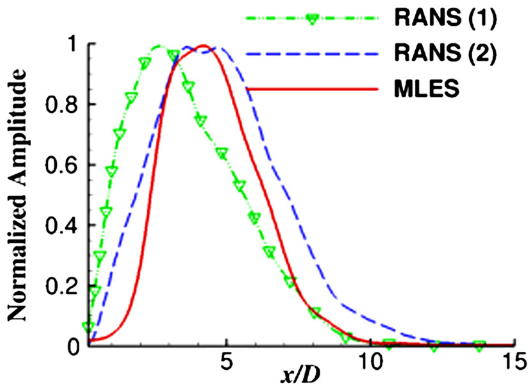

Fig. 24. Normalized amplitude of the $St = 0.5$ component plotted as a function of x/D at the lip-line. Here, RANS (1) and RANS (2) refer to the cases when eddy-viscosity μ_t is included and excluded, respectively while using RANS based base-flow for NS-MFP. The acronym MLES indicates NS-MFP analysis with mean of LES as the base-flow.

The use of a RANS-derived mean flow as well as the effect of considering or suppressing the eddy viscosity is shown in Fig. 23, where contours of time-harmonic disturbance pressure p' are plotted at two excitation Strouhal numbers, $St = 0.3$ and 1.0. Frames (a) and (c) depict the case when eddy-viscosity, μ_t, is included for disturbance evolution by NS-MFP while frames (b) and (d) consider disturbance propagation without the use of eddy viscosity. Clearly, when the eddy viscosity is suppressed, the results have similar qualitative form as those obtained from the LES-derived mean flow. The inclusion of eddy-viscosity lowers the amplitude of radiation without altering its directivity. This is consistent with the rationale that μ_t acts as a source of diffusion in the jet-shear layer (Fig. 22), which in turn damps the disturbance.

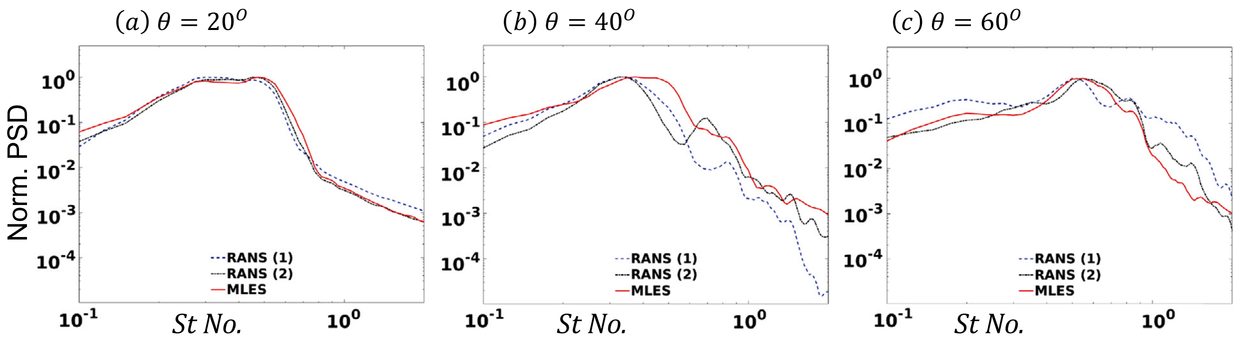

Fig. 25. Normalized power spectral density (PSD) plotted as a function of Strouhal number *St* at indicated polar angles. Here, RANS (1) and RANS (2) refer to the cases when eddy-viscosity μ_t is included and excluded, respectively while using RANS-based base-flow for NS-MFP. The acronym MLES indicates NS-MFP analysis with mean of LES as the base-flow.

To further quantitatively study the effects of using a base-flow from RANS, Fig. 24 depicts the streamwise variation of the normalized $St = 0.5$ amplitude for the three cases: RANS basic state with and without eddy viscosity as well as the LES basic state. The choice of $St = 0.5$ is dictated by prior results (Fig. 19) where the centerline variation of $St = 0.5$ component displays maximum amplitude among the four Strouhal numbers plotted. Here, we again plot and compare only the variation of the self-normalized amplitude to highlight the spatial characteristics of the response field on the eddy-viscosity. For reference, maximum amplitudes for the streamwise variation of the $St = 0.5$ component along the centerline are 0.015, 0.05 and 0.145, respectively for RANS-1 (when μ_t is included for NS-MFP with RANS-derived base-flow), RANS-2 (when μ_t is excluded for NS-MFP with RANS-derived base-flow) and MLES (NS-MFP with LES-derived base-flow) cases respectively, and are used for respective normalizations shown in Fig. 24. Fig. 24 indicates that the RANS simulation without μ_t yields the similar general behavior as LES-based solution in terms of the streamwise location of the maximum amplitude. Including μ_t shifts that location slightly upstream. The time-accurate LES of the Mach 1.3 jet displayed (Fig. 19), showed that for $St = 0.5$, the maximum amplitude of perturbations occur around $x/D \simeq 4$. These results suggest that the inclusion of μ_t leads to slight distortion of the resulting wave-packet but a large damping of the disturbance field. Therefore, it is not recommended in performing mean flow perturbations, based on these observations.

Finally, the spectral response with the LES and the two RANS cases is shown in Fig. 25 for different polar angles. The normalized (by the maximum PSD) value is plotted against Strouhal numbers. Several observations are apparent. All three cases display almost identical value of the peak Strouhal number (the value of *St* corresponding to maximum PSD), whose location moves to the right on the *St* axis. At the shallow angle direction of interest, $\theta = 20°$, results are almost identical for all the three cases and the rate of fall-off of the spectra at higher Strouhal numbers is also very similar. In general however, results with the LES mean flow and the RANS case without eddy viscosity are closer to each other – reiterating that there is no advantage in this situation to consider the eddy viscosity in the perturbation.

6. Summary and conclusion

The Navier–Stokes equation based mean flow perturbation method (NS-MFP) to derive modal responses from the linearized Navier–Stokes equations has been first verified by considering limiting cases of linear stability theory (LST), parabolized stability equation (PSE) or global stability theory (GST). Distinctions from other approaches which solve the disturbance form of the governing equations, including non-linear disturbance equations (NLDE), compact disturbance equation (CDE) and zero-average source term (ZAST) have been delineated and considerations regarding computational expense are provided. The entropy layer perturbation growth as estimated by LST is then verified by successfully reproducing linear inviscid stability results for three excitation frequencies in terms of wavelength, amplification and phase speed. Round jets at Mach 0.9 and 1.3 are then considered to establish the NS-MFP approach as a means to obtain elements of the near field. For the former, the NS-MFP results from the time-averaged basic state are compared with those from PSE. It is shown that a wave-packet structure arises for all excitations. The direct comparison with PSE results is performed with monochromatic and multi-frequency excitation. The monochromatic perturbation at a Strouhal number of 0.3, initiated with mode-shape functions obtained from local linear stability analysis indicates similar results when the basic state streamwise variation is adjusted to match the approximations made to converge the PSE. For the Mach 1.3 case, the disturbance evolution with NS-MFP reproduces some of the key features of the LES, including directivity associated with large scale structures and variation of spectra for moderate Strouhal number and shallow angles. A study of a RANS-derived basic state also yields similar results as the LES-derived state if the eddy viscosity is neglected in the evolution of the perturbations.

Conflict of interest statement

The authors of the manuscript certify that they have NO affiliations with or involvement in any organization or entity with any financial interest (such as honoraria; educational grants; participation in speakers' bureaus; membership, employment, consultancies, stock ownership, or other equity interest; and expert testimony or patent-licensing arrangements), or non-financial interest (such as personal or professional relationships, affiliations, knowledge or beliefs) in the subject matter or materials discussed in this manuscript.

Acknowledgements

SB was partly supported under an AFOSR task (FA9550-14-1-0167) monitored by Dr. I. Leyva and the Boeing Corporation (Contract No. 1085219). The simulations were performed with a grant of computer time from the DoD HPCMP DSRCs at AFRL, NAVO and ERDC, and the Ohio Supercomputer Center. Helpful discussions with M. Choudhari and M. Visbal are gratefully acknowledged. Several figures were made with Field-view licenses made available under the Intelligent Light University Partnership Program. AS acknowledges support from Industrial Research and Consultancy Center of Indian Institute of Technology Bombay, via the seed grant program.

Appendix A. Connection of NS-MFP to traditional methods

A.1. Relation to local linear stability approach

To evaluate the local stability of any given profile, the eigenvalues of the corresponding *Orr–Sommerfeld Equation* (OSE) are examined as described in Refs. [38–40,74,75]. The Orr–Sommerfeld equation is derived for the linearized evolution of disturbances under the assumption of parallel base-flow, *i.e.* it does not vary with respect to streamwise x- or spanwise/azimuthal coordinate z [38,75]. The coordinate y may refer to wall-normal direction for wall-bounded flows [74,75] or radial direction for axisymmetric flows such as round jets [39,51]. Under the parallel flow assumption, all the spatial derivatives of the base-flow W_b with respect to either x or z coordinate is zero and Eq. (16) transforms to

$$\begin{aligned}\frac{\partial W'}{\partial t} &= A_{11b}(W_b(y))\frac{\partial W'}{\partial x} + A_{12b}(W_b(y))\frac{\partial W'}{\partial y}\\ &\quad + A_{13b}(W_b(y))\frac{\partial W'}{\partial z} + W'\,\frac{\partial B_{12b}(W_b)}{\partial y} + \tilde{C}_{11b}\frac{\partial^2 W'}{\partial x^2}\\ &\quad + \tilde{C}_{12b}\frac{\partial^2 W'}{\partial y^2} + \tilde{C}_{13b}\frac{\partial^2 W'}{\partial z^2} + \tilde{C}_{14b}\frac{\partial^2 W'}{\partial x\partial y}\\ &\quad + \tilde{C}_{15b}\frac{\partial^2 W'}{\partial x\partial z} + \tilde{C}_{16b}\frac{\partial^2 W'}{\partial y\partial z} \qquad \text{(A.1)}\end{aligned}$$

In Eq. (A.1), the matrices $\tilde{C}_{..b}$ are obtained from corresponding $C_{..b}$ matrix by neglecting x and z derivatives of the base-flow. The small perturbation may be expressed by its Fourier–Laplace transform as

$$\begin{aligned}&W'(x,y,z,t)\\ &= \left(\frac{1}{2\pi}\right)^3 \int_\omega\int_\beta\int_\alpha \widetilde{W'_L}(\alpha,\beta,\omega;y)e^{i(\alpha x+\beta z-\omega t)}\,d\alpha\,d\beta\,d\omega \quad \text{(A.2)}\end{aligned}$$

Inserting Eq. (A.2) in Eq. (A.1), the governing equation for $\widetilde{W'_L}$ becomes:

$$\mathcal{A}_b\widetilde{W'_L} + \mathcal{B}_b\frac{d\widetilde{W'_L}(y)}{dy} + \tilde{C}_{12b}\frac{d^2\widetilde{W'_L}(y)}{dy^2} = 0 \qquad \text{(A.3)}$$

where

$$\begin{aligned}\mathcal{A}_b = \Bigg(&i\alpha A_{11b}(y) + i\beta A_{13b}(y) + i\omega + \frac{dB_{12b}(y)}{dy}\\ &- \alpha^2\tilde{C}_{11b} - \beta^2\tilde{C}_{13b} - \alpha\beta\tilde{C}_{15b}\Bigg)\end{aligned}$$

and

$$\mathcal{B}_b = \left(A_{12b}(y) + i\alpha\tilde{C}_{14b} + i\beta\tilde{C}_{16b}\right)$$

This recovers the *Orr–Sommerfeld equation* used in local linear stability analysis. For the eigenvalue analysis, this equation is subjected to appropriate homogeneous boundary conditions for $\widetilde{W'_L}$.

A.2. Relation to parabolized stability equations (PSE)

In the PSE based approach [3,4], the base-flow W_b is considered to be slowly varying along the streamwise coordinate x. Therefore, $W_b = W_b(X,y)$, where $X = \epsilon x$ is a slow function of x, *i.e.*, $0 < \epsilon \ll 1$. For a laminar wall bounded shear layer, $\epsilon = {Re_x}^{-1/2}$, where $Re_x = U_\infty x/\nu$ is the Reynolds number based on local streamwise coordinate x. The disturbance W' can be decomposed into Fourier modes as a product of a slowly varying shape function and a rapidly varying wave-like part in the axial direction as

$$\begin{aligned}W'(x,y,z,t) &= \left(\frac{1}{2\pi}\right)^2 \int_\omega\int_\beta \widetilde{W'_P}(\beta,\omega;X,y)\\ &\qquad \exp\left\{i\left(\int_{x_0}^{x}\alpha(\xi)d\xi + \beta z - \omega t\right)\right\}d\beta\,d\omega \qquad \text{(A.4)}\end{aligned}$$

It is to be pointed out that in Eq. (A.4), the complex wave-number α is a function of the slowly-varying streamwise coordinate X, *i.e.* $\alpha = \alpha(X)$. Substituting Eq. (A.4) in Eq. (16), the equation for $\widetilde{W'_P}$ becomes

$$\begin{aligned}&\mathcal{A}_b\widetilde{W'_P} + \mathcal{B}_b\frac{\partial\widetilde{W'_P}}{\partial y} + \tilde{C}_{12b}\frac{\partial^2\widetilde{W'_P}}{\partial y^2} + \epsilon\Bigg[\mathcal{C}_b\frac{\partial\widetilde{W'_P}}{\partial X} + \widetilde{W'_P}\frac{\partial B_{11b}}{\partial X}\\ &\quad + i\frac{d\alpha}{dX}C_{11b}\widetilde{W'_P} + C_{14b}\frac{\partial^2\widetilde{W'_P}}{\partial X\partial y}\Bigg] + \epsilon^2 C_{11b}\frac{\partial^2\widetilde{W'_P}}{\partial X^2} = 0 \qquad \text{(A.5)}\end{aligned}$$

where

$$\mathcal{C}_b = \left(A_{11b} + i\alpha(X)C_{11b} + i\beta C_{15b}\right)$$

Comparing Eq. (A.5) with Eq. (A.3), one can also alternatively express Eq. (A.5) up to $\mathcal{O}(\epsilon)$ as

$$\begin{aligned}&\mathcal{L}_0(\widetilde{W'_P}) + \epsilon\Bigg[\mathcal{C}_b\frac{\partial\widetilde{W'_P}}{\partial X} + \widetilde{W'_P}\frac{\partial B_{11b}}{\partial X} + i\frac{d\alpha}{dX}C_{11b}\widetilde{W'_P}\\ &\quad + C_{14b}\frac{\partial^2\widetilde{W'_P}}{\partial X\partial y}\Bigg] = 0 \qquad \text{(A.6)}\end{aligned}$$

where the operator $\mathcal{L}_0$ is given as

$$\mathcal{L}_0 = \left(\mathcal{A}_b + \mathcal{B}_b\frac{\partial}{\partial y} + \tilde{C}_{12b}\frac{\partial^2}{\partial y^2}\right)$$

Equation (A.6) is effectively the PSE for the corresponding flow. However, Eq. (A.6) alone is not sufficient to obtain an axial variation of the shape function $\widetilde{W'_P}$ and the complex wavenumber α. This is because the decomposition (A.4) does not resolve the ambiguity in the slow-axial variation which can be subsumed either in $\widetilde{W'_P}$ or α [3]. To address this issue additional integral constraints are generally used on the shape function $\widetilde{W'_P}$ [3].

Although the correspondence to PSE has been established, direct comparisons with NS-MFP is constrained by practical considerations. Stability constraints for the PSE marching require that the corresponding mesh has to be considerably coarser than NS-MFP, where the numerical technique is susceptible to serious issues with truncation error for such coarse meshes. Secondly, derivation of PSE assumes that the mean flow is a solution, while NS-MFP enforces this constraint explicitly. When the basic state is not a solution of the NS equations or the gradient of the base flow is not small enough, the results from the two approaches can differ as illustrated in Sec. 5.1. For such cases, one needs to take additional measures to match predictions of disturbance evolution from these two approaches. A similar measure has been taken in Sec. 5.1, where the streamwise gradient of the base-flow is artificially smoothed so that amplitude variation of both cases can be favorably matched. Therefore, the use of PSE necessarily requires restraining assumptions which NS-MFP does not.

A.3. Relation to global stability equation

If the imposed perturbations are small, the nonlinear terms in Eq. (3) may be neglected. For temporal instability analysis, $W' = W'_0 e^{i\omega t}$ where $\omega = \omega_r + i\omega_i$ with ω_r denoting the frequency of oscillation and ω_i denoting temporal growth rate of the disturbances. For Global Stability Analysis [41], $\partial W'/\partial x = [P]W'$, $\partial W'/\partial y = [R]W'$ and $\partial W'/\partial z = [S]W'$, where the matrices P, R and S result from the spatial discretization schemes adopted to numerically evaluate the derivatives along x-, y- and z-directions, respectively. Upon substituting these in Eq. (16) and further simplifying, the following eigenvalue problem is obtained in terms of complex ω as

$$\hat{A}W'_0 = i\omega W'_0 \tag{A.7}$$

This is the same as the *Global Stability Equation* as discussed in Ref. [1] and [41] and used to analyze the evolution of disturbances by Alizard and Robinet [76], Ehrenstein and Gallaire [77], Nichols and Lele [78] and other references contained therein.

References

[1] V. Theofilis, Global linear instability, Annu. Rev. Fluid Mech. 43 (2011) 319–352.
[2] T. Herbert, F. Bertolotti, Stability analysis of nonparallel boundary layers, Bull. Am. Phys. Soc. 32 (1987) 2079.
[3] T. Herbert, Parabolized stability equations, Annu. Rev. Fluid Mech. 29 (1997) 245–283.
[4] F.P. Bertolotti, T. Herbert, Analysis of the linear stability of compressible boundary layers using the PSE, Theor. Comput. Fluid Dyn. 3 (1991) 117–124.
[5] F. Bertolotti, T. Herbert, P. Spalart, Linear and nonlinear stability of the Blasius boundary layer, J. Fluid Mech. 242 (1992) 441–474.
[6] F. Li, M.R. Malik, Spectral analysis of parabolized stability equations, Comput. Fluids 26 (3) (1997) 279–297.
[7] P. Andersson, D. Henningson, A. Hanifi, On a stabilization procedure for the parabolic stability equations, J. Eng. Math. 33 (3) (1998) 311–332.
[8] A. Sinha, D. Rodriguez, G.A. Bres, T. Colonius, Wavepacket models for supersonic jet noise, J. Fluid Mech. 742 (2014) 71–95.
[9] N.D. Sandham, A.M. Salgado, Nonlinear interaction model of subsonic jet noise, Philos. Trans. R. Soc. Lond. A, Math. Phys. Eng. Sci. 366 (1876) (2008) 2745–2760.
[10] T.S. Haynes, H.L. Reed, Simulation of swept-wing vortices using nonlinear parabolized stability equations, J. Fluid Mech. 405 (2000) 325–349.
[11] A. Sinha, K. Gudmundsson, H. Xia, T. Colonius, Parabolized stability analysis of jets from serrated nozzles, J. Fluid Mech. 789 (2016) 36–63.
[12] R. Pierrehumbert, S. Widnall, The two- and three-dimensional instabilities of a spatially periodic shear layer, J. Fluid Mech. 114 (1982) 59–82.
[13] V. Theofilis, Advances in global linear instability analysis of nonparallel and three-dimensional flows, Prog. Aerosp. Sci. 39 (4) (2003) 249–315.
[14] I. Galionis, P. Hall, Spatial stability of the incompressible corner flow, Theor. Comput. Fluid Dyn. 19 (2) (2005) 77–113.
[15] N. De Tullio, P. Paredes, N. Sandham, V. Theofilis, Laminar–turbulent transition induced by a discrete roughness element in a supersonic boundary layer, J. Fluid Mech. 735 (2013) 613–646.
[16] A. Towne, T. Colonius, One-way spatial integration of hyperbolic equations, J. Comput. Phys. 300 (2015) 844–861.
[17] B. Ganapathisubramani, N. Clemens, D. Dolling, Low-frequency dynamics of shock-induced separation in a compression ramp interaction, J. Fluid Mech. 636 (2009) 397–425.
[18] P. Dupont, S. Piponniau, A. Sidorenko, J. Debieve, Investigation by particle image velocimetry measurements of oblique shock reflection with separation, AIAA J. 46 (2008) 1365–1370.
[19] K.J. Plotkin, Shock wave oscillation driven by turbulent boundary-layer fluctuations, AIAA J. 13 (1975) 1036–1040.
[20] E. Touber, N. Sandham, Low-order stochastic modelling of low-frequency motions in reflected shock-wave/boundary-layer interactions, J. Fluid Mech. 671 (2011) 417–465.
[21] E. Touber, N.D. Sandham, Large eddy simulation of low-frequency unsteadiness in a turbulent shock-induced separation bubble, Theor. Comput. Fluid Dyn. 23 (2009) 79–107.
[22] C.K. Tam, Supersonic jet noise, Annu. Rev. Fluid Mech. 27 (1) (1995) 17–43.
[23] P.J. Morris, M.G. Giridharan, G.M. Lilley, On the turbulent mixing of compressible free shear layers, Proc. R. Soc. Lond., Ser. A, Math. Phys. Eng. Sci. 431 (1990) 219–243.
[24] C.K. Tam, P. Chen, Turbulent mixing noise from supersonic jets, AIAA J. 32 (9) (1994) 1774–1780.
[25] K. Viswanathan, P. Morris, Predictions of turbulent mixing in axisymmetric compressible shear layers, AIAA J. 30 (6) (1992) 1529–1536.
[26] T.C.K. Gudmundsson, Instability wave models for the near-field fluctuations of turbulent jets, J. Fluid Mech. 689 (2011) 97–128.
[27] A. Sinha, H. Alkandry, M. Kearney-Fischer, M. Samimy, T. Colonius, The impulse response of a high-speed jet forced with localized arc filament plasma actuators, Phys. Fluids 24 (2013) 125104.
[28] V. Suponitsky, N.D. Sandham, C.L. Morfey, Linear and nonlinear mechanisms of sound radiation by instability waves in subsonic jets, J. Fluid Mech. 658 (2010) 509–538.
[29] M.E. Goldstein, A generalized acoustic analogy, J. Fluid Mech. 488 (2003) 315–333.
[30] R.R. Mankbadi, R. Hixon, S.H. Shih, L.A. Povinelli, Use of linearized Euler equations for supersonic jet noise prediction, AIAA J. 36 (2) (1998) 140–147.
[31] Y. Du, P.J. Morris, Compact disturbance equations for aeroacoustic simulations, AIAA J. 54 (1) (2015) 77–87.
[32] R. Hixon, On the numerical calculation of nonlinear residual equations, Int. J. Aeroacoust. 14 (3–4) (2015) 607–641.
[33] P.J. Morris, L.N. Long, A. Bangalore, Q. Wang, A parallel three-dimensional computational aeroacoustics method using nonlinear disturbance equations, J. Comput. Phys. 133 (1) (1997) 56–74.
[34] M. Waindim, S. Bhaumik, D.V. Gaitonde, Further development of the Navier–Stokes equations-based mean flow perturbation technique, in: 54th AIAA Aerospace Sciences Meeting, 2016, p. 1816.
[35] D.V. Gaitonde, Progress in shock wave/boundary layer interactions, Prog. Aerosp. Sci. 72 (2015) 80–99.
[36] J. Crouch, A. Garbaruk, D. Magidov, Predicting the onset of flow unsteadiness based on global instability, J. Comput. Phys. 224 (2) (2007) 924–940.
[37] D.J. Garmann, M.R. Visbal, P.D. Orkwis, Comparative study of implicit and subgrid-scale model large-eddy simulation techniques for low-Reynolds number airfoil applications, Int. J. Numer. Methods Fluids 71 (12) (2013) 1546–1565.
[38] P.G. Drazin, W.H. Reid, Hydrodynamic Stability, Cambridge Univ. Press, Cambridge, UK, 1981.
[39] M.R. Malik, R.E. Spell, On the stability of compressible flow past axisymmetric bodies, J. Fluid Mech. 228 (1991) 443–463.
[40] M.R. Malik, S.A. Orszag, Linear stability analysis of three-dimensional compressible boundary layers, J. Sci. Comput. 2 (1) (1987) 77–97.
[41] M.P. Juniper, A. Hanifi, V. Theofilis, Modal Stability Theory, Lecture notes from the FLOW-NORDITA Summer School on Advanced Instability Methods for Complex Flows, Stockholm, Sweden, 2013.
[42] A. Fedorov, A. Tumin, Evolution of disturbances in entropy layer on a blunted plate in supersonic flow, AIAA Paper 2002-2847.
[43] J. Yakura, Theory of Entropy Layers and Nose Blunting in Hypersonic Flow, Academic Press, New York, 1962, Ch. Hypersonic Flow Research.
[44] M. van Dyke, Perturbation Methods in Fluid Mechanics, Academic Press, New York, 1964.
[45] D. Gaitonde, J. Shang, J. Young, Practical aspects of higher-order numerical schemes for wave propagation phenomena, Int. J. Numer. Methods Eng. 45 (1999) 1849–1869.
[46] S. Conte, C. de Boor, Elementary Numerical Analysis – An Algorithmic Approach, McGraw–Hill Book Company, 1980.
[47] D. González, R. Speth, D. Gaitonde, M. Lewis, Finite-time Lyapunov exponent-based analysis for compressible flows, Chaos, Interdiscip. J. Nonlinear Sci. 26 (8) (2016) 083112.
[48] R. Speth, D. Gaitonde, Parametric study of a supersonic jet subjected to plasma-based flapping mode excitation, AIAA Paper 2012-0901.
[49] D. Gaitonde, M. Samimy, Coherent structures in plasma-actuator controlled supersonic jets: axisymmetric and mixed azimuthal modes, Phys. Fluids 23 (9) (2011).
[50] J.C. Hunt, A.A. Wray, P. Moin, Eddies, streams, and convergence zones in turbulent flows, in: Proceedings of the 1988 Summer Program, Center for Turbulence Research, Stanford University.
[51] P.J. Morris, Viscous stability of compressible axisymmetric jets, AIAA J. 21 (4) (1983) 481–482.
[52] S.B. Müller, L. Kleiser, Viscous and inviscid spatial stability analysis of compressible swirling mixing layers, Phys. Fluids (1994–present) 20 (11) (2008) 114103.
[53] Y.B. Baqui, A. Agarwal, A.V. Cavalieri, S. Sinayoko, A coherence-matched linear source mechanism for subsonic jet noise, J. Fluid Mech. 776 (2015) 235–267.
[54] M.R. Visbal, D.V. Gaitonde, High-order-accurate methods for complex unsteady subsonic flows, AIAA J. 37 (10) (1999) 1231–1239.
[55] P. Jordan, T. Colonius, Wave packets and turbulent jet noise, Annu. Rev. Fluid Mech. 45 (2013) 173–195.
[56] F. Li, M.R. Malik, On the nature of PSE approximation, Theor. Comput. Fluid Dyn. 8 (4) (1996) 253–273.
[57] H. Haj-Hariri, Characteristics analysis of the parabolized stability equations, Stud. Appl. Math. 92 (1) (1994) 41–53.
[58] R. Speth, D.V. Gaitonde, Parametric study of a Mach 1.3 cold jet excited by the flapping mode using plasma actuators, Comput. Fluids 84 (2013) 16–34.

[59] S. Unnikrishnan, D.V. Gaitonde, Acoustic, hydrodynamic and thermal modes in a supersonic cold jet, J. Fluid Mech. 800 (2016) 387–432.

[60] C.K. Tam, M. Golebiowski, J.M. Seiner, On the Two Components of Turbulent Mixing Noise from Supersonic Jets, American Institute of Aeronautics and Astronautics, 1996.

[61] A.V.G. Cavalieri, D. Rodriguez, P. Jordan, T. Colonius, Y. Gervais, Wavepackets in the velocity field of turbulent jets, J. Fluid Mech. 730 (2013) 559–592.

[62] D.E. Breakey, P. Jordan, A.V. Cavalieri, O. Léon, M. Zhang, G. Lehnasch, T. Colonius, D. Rodrıguez, Near-field wavepackets and the far-field sound of a subsonic jet, in: 19th AIAA/CEAS Aeroacoustics Conference, Berlin, Germany, in: AIAA Paper, vol. 2083, 2013.

[63] A.V. Cavalieri, P. Jordan, A. Agarwal, Y. Gervais, Jittering wave-packet models for subsonic jet noise, J. Sound Vib. 330 (18) (2011) 4474–4492.

[64] C.K. Tam, D.E. Burton, Sound generated by instability waves of supersonic flows. Part 2. Axisymmetric jets, J. Fluid Mech. 138 (1984) 273–295.

[65] C.K. Tam, K. Viswanathan, K. Ahuja, J. Panda, The sources of jet noise: experimental evidence, J. Fluid Mech. 615 (1) (2008) 253–292.

[66] D. Rodríguez, A. Sinha, G.A. Brès, T. Colonius, Inlet conditions for wave packet models in turbulent jets based on eigenmode decomposition of large eddy simulation data, Phys. Fluids 25 (10) (2013) 105107.

[67] B. Launder, B. Sharma, Application of the energy-dissipation model of turbulence to the calculation of flow near a spinning disc, Lett. Heat Mass Transf. 1 (2) (1974) 131–137.

[68] D. Rizzetta, Numerical simulation of vortex-induced oblique shock-wave distortion, AIAA J. 35 (1) (1997) 209–211.

[69] W. Reynolds, A. Hussain, The mechanics of an organized wave in turbulent shear flow. Part 3. Theoretical models and comparisons with experiments, J. Fluid Mech. 54 (02) (1972) 263–288.

[70] Y. Lifshitz, D. Degani, A. Tumin, On the interaction of turbulent shear layers with harmonic perturbations, Flow Turbul. Combust. 80 (1) (2008) 61–80.

[71] S. Pirozzoli, J. Larsson, J. Nichols, M. Bernardini, B. Morgan, S. Lele, Analysis of unsteady effects in shock/boundary layer interactions, Annu. Res. Briefs (2010) 153–164.

[72] M. Gaster, E. Kit, I. Wygnanski, Large-scale structures in a forced turbulent mixing layer, J. Fluid Mech. 150 (1985) 23–39.

[73] K. Oberleithner, M. Sieber, C. Nayeri, C. Paschereit, C. Petz, H.-C. Hege, B. Noack, I. Wygnanski, Three-dimensional coherent structures in a swirling jet undergoing vortex breakdown: stability analysis and empirical mode construction, J. Fluid Mech. 679 (2011) 383–414.

[74] L.M. Mack, Boundary-Layer Linear Stability Theory, AGARD Report 709, 1984.

[75] H.L. Reed, W.S. Saric, D. Arnal, Linear stability theory applied to boundary layers, Annu. Rev. Fluid Mech. 28 (1996) 389–428.

[76] F. Alizard, J. Robinet, Spatially convective global modes in a boundary layer, Phys. Fluids 19 (2007) 114105.

[77] U. Ehrenstein, F. Gallaire, Two-dimensional global low-frequency oscillations in a separating boundary-layer flow, J. Fluid Mech. 614 (2008) 315–327.

[78] J.W. Nichols, S.K. Lele, Global modes and transient response of a cold supersonic jet, J. Fluid Mech. 669 (2011) 225–241.